

Building a Safer Maritime Environment Through Multi-Path Long-Term Vessel Trajectory Forecasting

Gabriel Spadon^{1,2,♦}, Jay Kumar^{1,♦}, Matthew Smith¹,
Sarah Vela¹, Romina Gehrmann¹, Derek Eden³, Josh van Berkel³,
Amilcar Soares⁴, Ronan Fablet², Ronald Pelot⁵, and Stan Matwin^{1,6}

¹ Institute for Big Data Analytics, Dalhousie University, Halifax – NS, Canada

² Département Mathematical and Electrical Engineering, IMT Atlantique, Brest, France

³ DHI Water & Environment Inc., Ottawa, Canada

⁴ Department of Computer Science and Media Technology, Linnaeus University, Växjö, Sweden

⁵ Industrial Engineering Department, Dalhousie University, Halifax – NS, Canada

⁶ Institute of Computer Science, Polish Academy of Sciences, Warsaw, Poland

♦ These authors contributed equally to this work.

Corresponding author: gabriel@spadon.com.br

ABSTRACT

Maritime transportation is paramount in achieving global economic growth and preserving environmental sustainability. In this regard, the Automatic Identification System (AIS) data plays a significant role by offering real-time streaming data on vessel movement, which allows for enhanced traffic surveillance, assisting in vessel safety by avoiding vessel-to-vessel collisions and proactively preventing vessel-to-whale ones. This paper tackles an intrinsic problem to trajectory forecasting: the effective multi-path long-term vessel trajectory forecasting on engineered sequences of AIS data. For such a task, we have developed an encoder-decoder model architecture using Bidirectional Long Short-Term Memory Networks (Bi-LSTM) to predict the next 12 hours of vessel trajectories using 1 to 3 hours of AIS data as input. We feed the model with probabilistic features engineered from the AIS data that refer to the potential route and destination of each trajectory so that the model, leveraging convolutional layers for spatial feature learning and a position-aware attention mechanism that increases the importance of recent timesteps of a sequence during temporal feature learning, forecasts the vessel trajectory taking the potential route and destination into account. The probabilistic features have an F1 Score of approximately 85% and 75% for each feature type, respectively, demonstrating their effectiveness in augmenting information to the neural network. We test our model on the Gulf of St. Lawrence, a region known to be the habitat of North Atlantic Right Whales (NARW). Our model achieved an R^2 score of over 98% in different techniques using varying features. The high R^2 score is a natural outcome of the well-defined shipping lanes. However, our model stands out among state-of-the-art ones as it demonstrates the capability of complex decision-making during path selection. Also, we have shown that our model can achieve more accurate forecasting in terms of average and median forecasting errors, with 11km and 6km, respectively. Overall, our study demonstrates the potential of geographical data engineering and trajectory forecasting models for marine life species preservation.

Introduction

Maritime transportation plays a vital role in global economic development and environmental sustainability. The International Maritime Organization (IMO) was established to encourage and implement policies related to maritime safety, navigation efficiency, and the prevention of marine pollution by ships¹. Its primary function is to improve traffic surveillance and vessel safety by providing real-time information about vessel movement². The Automatic Identification System (AIS) is a technology used to track the location of marine vessels worldwide, and according to Canadian regulations (Section 65 of the Navigation Safety Regulations¹), every Canadian or foreign vessel heading to Canada is required to have an AIS transceiver that can provide information about its route and receive information about nearby vessels. With the help of terrestrial and satellite receivers, we can capture transmissions and track vessels,

¹ Available at: <https://laws-lois.justice.gc.ca/eng/regulations/SOR-2020-216>

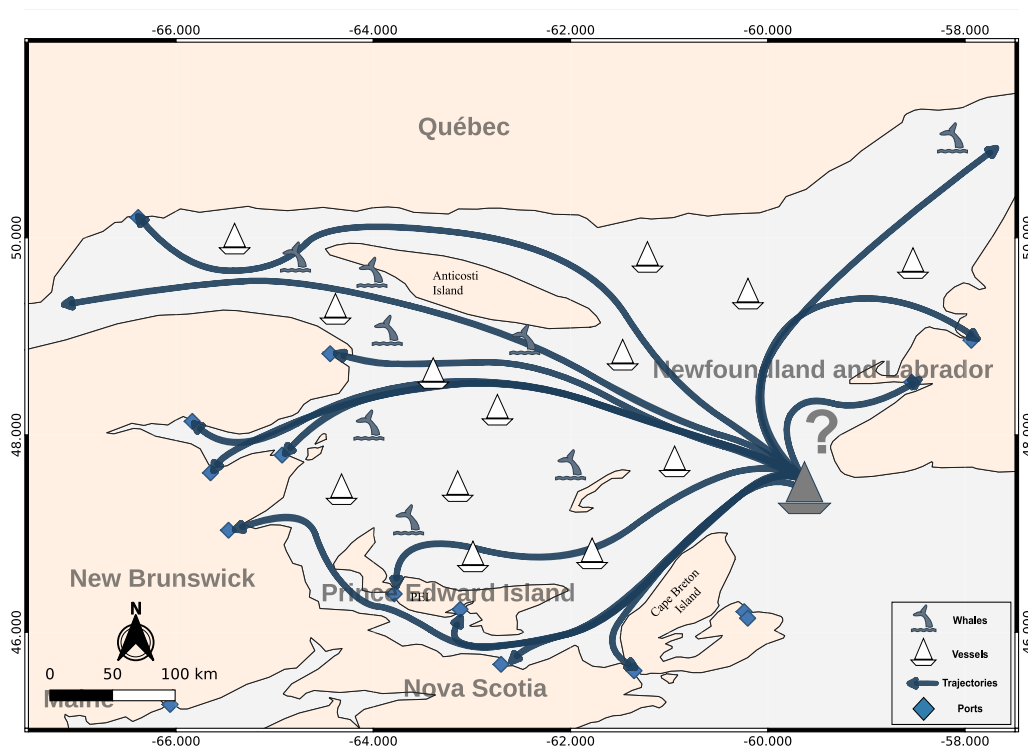


Figure 1. Visual representation of a vessel path decision in the Gulf of St. Lawrence, given the high vessel traffic in the region and the uncertainty of marine life positioning along the many possible routes. The image shows a vessel entering the gulf using the straight between Cape Breton Island in Nova Scotia (NS) and Mouse Island in Newfoundland and Labrador (NL). There are many possible destinations, including ports in Quebec (QC) and New Brunswick (NB), besides the ones in NS and NL. A vessel can anchor in one of these ports, go deeper in the gulf using the St. Lawrence River, or exit it on the straight between St. Barbe (NL) and Blanc Sablon (QC), such that many of these possibilities can be achieved using different paths, meaning a vessel can have a common start and end for a trajectory but a different route each time.

improving our awareness of the oceans through its two-way communication system. This technology is beneficial not only for individual vessel tracking but also for shore-based facilities like the Coast Guard's Marine communications and traffic services, which can remotely monitor collective traffic and individual movements, acting to prevent distress situations^{3–5}, such as collisions in the route (see Figure 1).

AIS messages are transmitted in an encoded format, and among the content transmitted, the most common and relevant to this paper are the vessel coordinates (Longitude and Latitude); besides those, an AIS message also provides Speed over Ground (SOG), Course over Ground (COG), timestamps, identification information (*e.g.*, Maritime Mobile Service Identity — MMSI and/or IMO identifiers) and vessel dimensions (*e.g.*, width and height) within its content. These messages are transmitted by most vessels every 2–10 seconds or 3–5 minutes, depending on the status, qualifications, and purposes of the vessel^{6,7}. The vast amount of data broadcasted worldwide, with approximately 500–600 million messages per day⁸, has become the source of constructing AIS datasets. These datasets contain spatial-temporal data and have been widely exploited for applications that require the analysis of mobility patterns and management of shipping routes^{8–13}. Handling AIS data can be complex because of the large amount of data involved, which contains messages that are damaged, duplicated, or otherwise incorrect^{14–16}.

The challenge of obtaining high-quality data is further impaired by the limited availability of freely accessible datasets. Open-source datasets often fail to meet the quality standards of paid or government-classified data sources, adding to the difficulty of cleaning, segmenting, and interpolating the data. Researchers in the scientific community have been struggling to develop efficient techniques and pipelines to address these issues and eliminate noise from the data^{17–19}. However, this remains an open challenge as most techniques are tailored to specific research projects and are not publicly available.

Research on AIS datasets has opened the doors to enhance maritime safety and security through solving various issues such as the detection of suspicious events²⁰, monitoring traffic to avoid collisions^{13,21}, and evaluating noise or environmental pollution levels^{22,23}. Recently, the problem of forecasting long-term trajectories^{24–27} of vessels gained significant attention to reduce vessel accidents, detect anomalous tracks, and improve path planning — especially for autonomous shipping^{28–34}. The study of trajectory forecasting has a diverse background, where different techniques have been employed to create models that predict movement, either from vessels or different vehicles. One of the most basic models is the constant velocity model, derived from the AIS messages' geographical coordinates and the vessel's SOG and COG at the last recorded timestep, assuming no change in speed and course for the forecasting duration. More refined models go beyond these assumptions and use the trajectory's geometry to produce more accurate predictions, such as the Ornstein–Uhlenbeck (OU) process adapted to vessel trajectory forecasting³⁵. In the past few years, there has been a significant advancement in machine learning and deep learning fields. These technologies have allowed for the creation of complex models that can combine different types of data beyond AIS on a multi-modality approach. However, the real-world use of these models is often limited in real-time scenarios due to the difficulty of synchronizing and preparing diverse data in streaming conditions. Therefore, research focusing on AIS messages and data for trajectory forecasting remains

valuable, as it has lightweight dependencies beyond the geographical coordinates of vessels, which are tied to the trajectory geometry and its trigonometrical traits. For instance, our proposal relies on the Latitude and Longitude of the vessel, whereas other features in our set are engineered based on those coordinates.

In a recent research study by Nguyen et al. (2021)³⁶, authors transformed the regression problem into classification and proposed an approach to represent four AIS-related features into embeddings, *i.e.*, a learned numerical representation of data where similar data points have a similar representation based on their meaning. Their study adopted the transformer encoder in a generative-driven approach to forecast long-term trajectory. However, their technique confines the ship's trajectory to the centroid of the grid-cells, and has three other main limitations. Firstly, models based on many classes require longer training sessions and are usually overly large, so it can learn the many patterns that distinguish each class uniquely when the data is correctly balanced across all classes. Secondly, paths limited to classified grid-cells' centroids can produce more straight trajectories than general routes. This approach may be effective when ships adhere to nearly constant velocity models, but its potential to learn more individual moving patterns is overlooked. Thirdly, the authors implemented their solution using teacher forcing³⁷ to improve the learning ability of their deep-learning model over sequences. In doing so, instead of inputting the previous step predictions as input to the next step, the technique trains the network with ground truth data as that information is known during the training phase. During testing, the network is rewired to revert the need for ground truth data, expecting that the learned weights during forced training will perform better in the testing phase. To be more specific, the authors feed-forward forecasted information about the speed and course of the vessel, which can instead be mathematically calculated when having information about two consecutive coordinates. Therefore, unless the model always provides a perfect estimation of the vessel's speed and course, the speed and course that is forwarded ahead in the model for predicting the next step of the sequence tends to be imprecise and does not accurately reflect the movement of the vessel.

In different studies, Capobianco et al. (2021)³⁸ and Capobianco et al. (2022)³⁹ have reviewed the effectiveness of recurrent encoder-decoder neural networks in trajectory forecasting. In both studies, the authors utilized comparable network architectures that employ an encoder to produce an embedding; this embedding is then utilized in an attention mechanism to allow for multi-step forecasting and take advantage of both short and long-term dependencies of the trajectories; and, the network decoder decodes the embedding and yields the forecasted trajectory. However, the issue in their modeling approach is not related to the auto-encoder model but rather to how the attention mechanism is employed. When attention is used over a sentence as seen in Large Language Models (LLMs) such as ChatGPT² or Bert³, the mechanism learns the significance (or importance) of words in the sentence, helping the model to focus on the key points of sentence and respond accordingly to the LLM operator. However, sequences of AIS messages and sentences (*i.e.*, sequences of words) have intrinsically different abstractions. In an AIS forecasting model, the knowledge that can be leveraged from the beginning of the sequence is considerably

² Available at: <https://openai.com/chatgpt>

³ Available at: <https://github.com/google-research/bert>

less important than the knowledge that can be extracted from later points in the same sequence because of the temporal and sequential nature of the data. This way, while the intermediate points of the sequence can aid in more accurate long-term trajectory forecasting, they also increase the uncertainty of the modeling problem in the short term because the model does not follow the correct order of events in the sequence.

Using a different approach, this paper advances previous works by using an equal-size hexagon grid for extracting probabilistic features that aid in identifying the vessel route and destination. These features allow for a finer approximation of the vessel path without being constrained by the centroids of the cells. This means that differently from Nguyen et al. (2021)³⁶, we tackle this problem in a regression rather than a classification fashion, where the ocean grid is a step to achieve the trajectory instead of being an anchor for the trajectories themselves. Through this approach, we developed a model that can predict 12 hours of AIS data based on 1 to 3 hours of input data, where 1 AIS message is sent every 10 minutes. The study focuses on the Gulf of St. Lawrence in Canada, where vessels can take different routes to reach various regional ports. The starting and ending points of each trajectory are known, and the purpose is to identify the paths that Cargo and Tanker vessels will take in an area with many destinations (see Figure 1).

To this end, we propose a spatio-temporal model instead of only benefiting from recurrent neural networks. The model has an encoder-decoder structure (see Figure 9) where the encoder has three stacked blocks of convolutional layers attached to a Bidirectional Long Short-Term Memory Network (Bi-LSTM). Each block has a pair of 1D convolutions (used for signals and series) where one extracts short-and the other longer-term dependencies from the input features. The stack of convolution blocks has parallel connections to enhance the gradient flow during training. Before moving forward with the Bi-LSTM decoding, our model includes a positional-aware attention mechanism, which differs from Capobianco et al. (2021)³⁸ and Capobianco et al. (2022)³⁹, resulting in a more accurate model for short-and-long-term AIS trajectory forecasting by allowing the auto-encoder model to learn from all AIS points in the trajectory but giving more importance to the latter timestep of the trajectory sequence. This technique involves the use of the attention mechanism as focal attention to the more recent AIS message reported by a vessel. This results in a smoother transition between inputs and outputs without requiring overly complex models.

To ensure the reproducibility of our work and cope with the challenge of dealing with erroneous and noisy messages from AIS data, we have developed a sophisticated tool called the Automatic Identification System Database (AISdb)⁴, introduced with more details in the methods section. Such a tool has been perfected over several years and is intended to foster research on AIS data in all fields by the scientific community. AISdb is an open-source⁵ platform that offers various tools for collecting and processing real-time and historical AIS data. It is highly flexible and compatible with live streaming and historical raw (*i.e.*, binary encoded) AIS data files. Its interface supports various operations, including creating databases, spatio-temporal querying, processing, visualizing, and exporting curated data. AISdb includes features that enable users to seamlessly integrate AIS data with environmental data stored in raster file

⁴ See <https://aisdb.meridian.cs.dal.ca/doc>.

⁵ See <https://git-dev.cs.dal.ca/meridian/aisdb/-/tree/master>.

formats. This enables users to merge multiple environmental data sources with AIS data, enhancing the analysis and interpretation of vessel movements and interactions with the marine environment.

As for the evaluation, we conducted an extensive set of experiments to test various scenarios and determine the effectiveness of our solution. We employed different sets of features and applied trigonometric transformations to them, using the results to train models with varying complexities. In such a case, we observed that the effectiveness in providing probabilistic information to the neural network is in the order of 85% and 75% of the F1 Score in predicting the route and the destination of the vessels, respectively. Those results represent the degree of certainty of the probabilistic features. Furthermore, our findings indicate that when using only coordinates, speed, course information, and their deltas (see Methods) to predict long-term trajectories, the model's ability to make path decisions is limited for both cargo and tanker vessels. This is due to the model's tendency to perform well on straight paths but struggle on complex and curved paths, resulting in mean and median errors of 13 km and 8 km, respectively, on the test dataset shared between both vessel types. Incorporating the proposed probabilistic features resulted in mean and median errors of 12 km and 8 km, respectively. However, after applying cartesian

⁶ See: <https://bit.ly/45DilrO>.

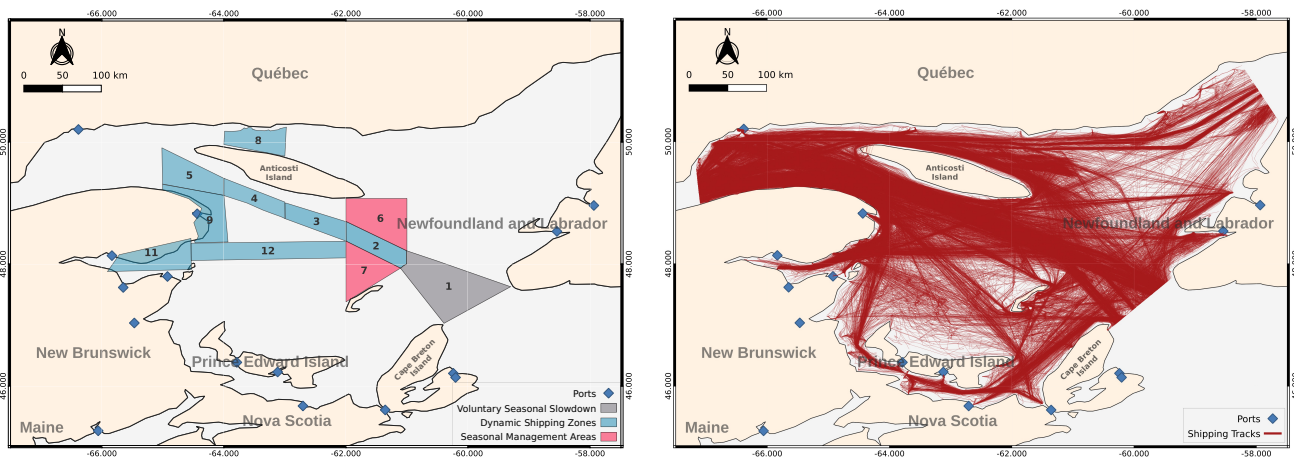


Figure 2. The Gulf of St. Lawrence, which is the area of interest of this study, contains traffic policy zones defined by Transport Canada⁶, as shown on the map on the left-hand side. This area includes voluntary seasonal slowdown, dynamic shipping zones, and seasonal management areas. The regulated areas overlay main vessel traffic routes, such as the one from the straight between Cape Breton Island in Nova Scotia and Mouse Island in Newfoundland and Labrador until the start of the St. Lawrence River (polygons 1–7). These areas also cover the ports zone between New Brunswick and Québec (polygons 9–11), besides the path between Anticosti Island and Mainland Québec (polygon 8). The visualization on the right-hand side shows the intensity of vessel trajectories in the same area, revealing that vessels do not follow consistent paths, even within shipping lanes. Most traffic occurs within regulated areas, so areas lacking traffic due to not being major routes for cargo and tanker vessels are less relevant to this study.

and other trigonometrical transformations to all sets of features, the errors were reduced further, resulting in mean and median errors of 11 km and 6 km. By using the trigonometrical transformations on the probabilistic features, we were able to achieve an R^2 score higher than 98% for cargo and tankers using the proposed model. Our contributions set a new milestone for long-term vessel trajectory forecasting using spatio-temporal data, probabilistic modeling of features, and advanced neural network techniques. These results have the potential to move forward with policies that can increase our awareness of the ocean, proactively aiding in reducing unintentional harm to endangered marine species, such as NARW.

Problem Formulation and Proposed Solution

This research is motivated by the increased maritime traffic in the Gulf of St. Lawrence (see Figure 2A), which poses a significant threat to the marine ecosystem, particularly to the North-Atlantic Right Whale (NARW) populations, which are often at risk of vessel-whale collisions. Developing effective strategies for managing vessel movement (see Figure 2B) and reducing the likelihood of collisions is essential to mitigate this risk. One promising approach in the face of the unpredictability of whales' movements is

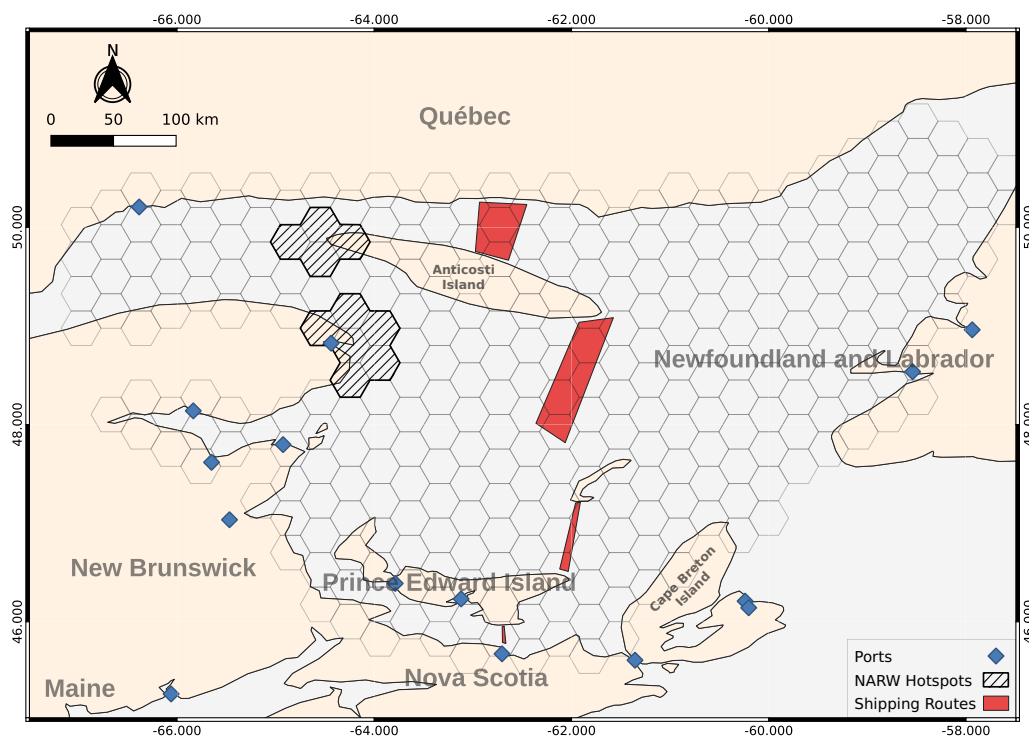


Figure 3. Area of interest with highlighted spots with hatched markers indicating hotspot for North Atlantic Right Whales (NARW)⁴⁰ and red polygons highlighting the four major routes a vessel can take. The route polygons segment the gulf from east to west, covering major inbound and outbound movements inside the gulf, but note that not all paths are required to cross a route polygon. Paths that cross route polygons tend to be easier to forecast, while the ones that do not pose more intricate forecasting scenarios.

to predict the vessel trajectory instead, which relies on advanced predictive models and real-time data to anticipate vessel paths that come across collision hotspot areas (see Figure 3A). As vessels navigate, their historical data provide us with insights into their likely trajectory besides observations on collective vessel movement patterns²¹; the same can be observed among people commuting^{41–43}, patient trajectories in hospitals^{44,45}, and spatio-temporal spreading phenomena^{46,47}. Accurately predicting the movement of vessels can provide valuable insights for authorities to identify and monitor areas with a high concentration of whales. This information can then be used to proactively adjust shipping routes and enforce speed restrictions in these areas, mitigating the risk of collisions and preserving the safety of marine life.

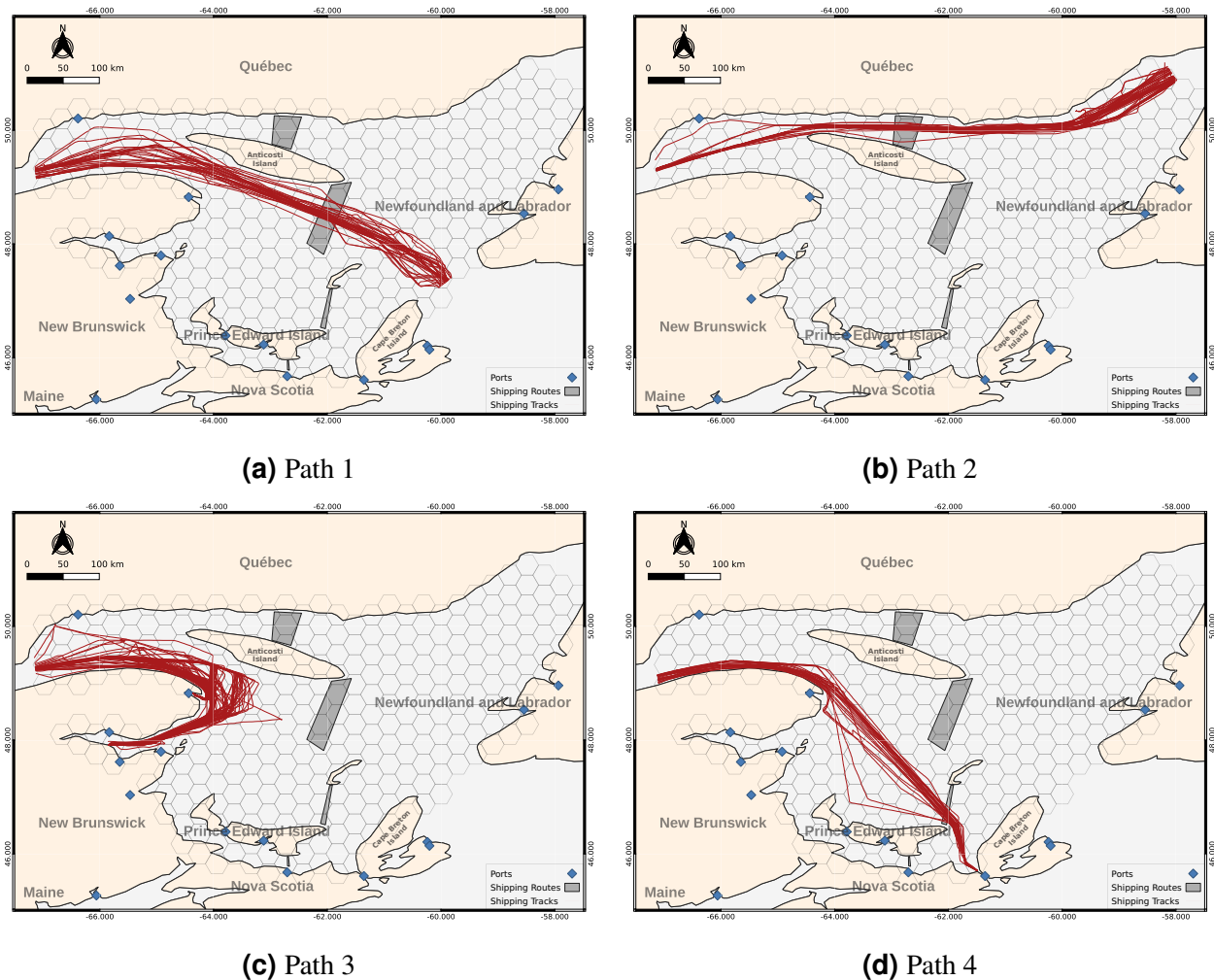


Figure 4. The Gulf of St. Lawrence region has multiple paths with high vessel traffic. However, the image only shows four of them, which is not a complete representation of all the trajectories in the dataset. Among these paths, we have three major ones (1, 2, and 4) that cross a route polygon either from east to west or vice versa. Path 3, on the other hand, does not intersect with any route polygon. Instead, it represents trajectories in key preservation areas and interacts with all major hotspots of NARW in the gulf.

The challenge we are addressing involves more than just the forecasting trajectories under the unpredictability of whales' locations. In the Gulf of St. Lawrence, ships can take various paths, even if their start and end are known beforehand (see Figure 3). This difficulty comes from the fact that, unlike city streets⁴⁸⁻⁵⁰, no physical grid directs ships into specific lanes. Although traffic management policies designate shipping lanes, the lanes do not restrict the movement of vessels as they may enter or exit lanes at different points throughout the gulf. As a result, predicting ship trajectories becomes challenging, especially for longer distances, as the predicted paths deviate significantly from actual paths with increased elapsed time and travel distance. Therefore, we require a deep-learning model that can learn from the input AIS data and its surroundings to understand the relationship between mobility constraints and patterns.

To solve this problem, we first split the gulf into hexagonal grid-cells (see Figure 3) of 0.3° on EPSG:4269⁷ projection. The shape of the cells is due to the Earth's curvature, as hexagonal cells are able to divide the Earth's surface uniformly. Figure 4 shows some paths discovered from historical data, highlighted by polygons placed in high-traffic areas. The reason for utilizing grid-cells is due to the fact that the AIS data does not always provide detailed information regarding the destination of a vessel's trajectory. In addition, there are countless possible locations for vessels in the gulf, making it difficult to compare them with others that have different, but yet similar, trajectories. Using grid-cells helps us to overcome these challenges and allows for a more effective comparison between vessels that pass through

⁷ See: <https://epsg.io/4269>.

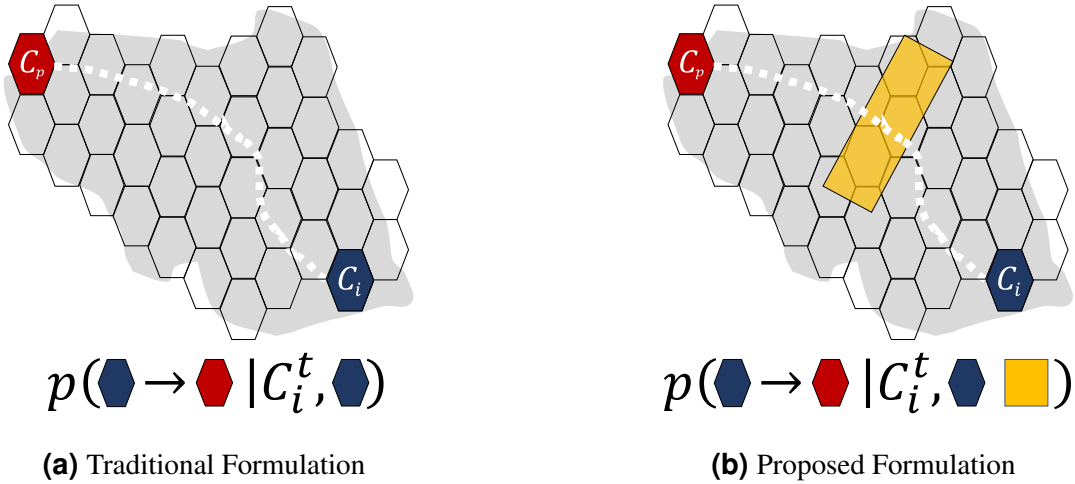


Figure 5. Probabilistic formulations of long-term trajectory forecasting. In the traditional method, a probabilistic matrix is utilized to determine the most likely whereabouts of a vessel by analyzing its movements concerning its starting point on a grid using historical data. Our proposed approach follows a similar method but with new features and a revisited understanding. In addition to historical data, we take into consideration their interaction with route polygons that overlay the gulf. Essentially, our model employs route-polygons as a type of memory to provide more precise guidance on the vessel's decisions at different moments in the past, ultimately leading to a more reliable and effective probabilistic system.

the same grid-cell. In this sense, comparing trajectories and the route polygons we placed in high-traffic areas, we can see that most trajectories intersect with route polygons at some point during their course. However, paths like the one in Figure 4C are the most challenging ones in the dataset as it does not intersect with any route polygons and represent a curvy-shaped moving pattern. With the probable routes identified as polygons and the gulf divided into grids, we developed a probabilistic model (see Algorithm 1) that leverages the relationship between grid-cells, polygons, and historical vessel track to predict the potential route a vessel will take and the probable destination (*i.e.*, last grid-cell) where the voyage will end. For the sake of disambiguation, this research uses two models, one for engineering features and referred to as the *probabilistic model*, and another one to forecast the trajectories, referred to as the *deep-learning model*.

Our proposal goes beyond traditional probabilistic forecasting, such as in Figure 5A, as we consider the interaction of the trajectories with route-related polygons that highlight major paths in the gulf, such as seen in Figure 5B. Additionally, our proposal assumes that the relationship between grid-cells and route polygons allows the deep-learning model to learn from its surroundings, and such additional information supports the model in deciding the correct path and turning points of each trajectory in the dataset. In this sense, the destination and route information provided by the probabilistic model guides the path decision, and the deep-learning model can then approximate the 12-hour trajectory of the vessel with less uncertainty when compared to the observed trajectory. In this configuration, tracks (*i.e.*, trajectories) have predetermined start and end locations. Therefore, the deep-learning model is intended to fill the gaps between the starting and ending locations of a track based on its segments, which (1) might not have started from the starting grid-cell and (2) might not achieve the target destination cell at the end of forecasting. That is because the complete displacement might have a longer duration than 15 hours (*i.e.*, 1 to 3 hours of input and 12 hours of output), and the deep-learning model is trained on slices of tracks.

Understanding the movements and patterns of vessels is essential in this approach, and analyzing the data collected from their tracks is crucial. By calculating the number of tracks going to a particular destination, the direction of each track at the point where it intersects with a route polygon, and the probability score of each surrounding cell as a potential destination for each track, we can gain valuable insights into ship behavior and the routes they take. The primary objective of this approach is to predict the likely destination while considering the vessel's current position. This is achieved by calculating the Euclidean distance between the current motion behavior of the vessel and the historical movement of vessels in the same grid-cell for each possible grid-cell destination. We take into consideration grid information and AIS messages to determine probability scores and potential destinations for a vessel. The output of this process is engineered features to the problem of long-term multi-path trajectory forecasting.

Pipeline Overview

Our trajectory forecasting pipeline, in Figure 6, begins by extracting crucial information from the AIS messages, which includes the time, vessel type, and location. These messages are grouped based on the unique vessel identification number (MMSI). Messages of each vessel are then interpolated 10 minutes

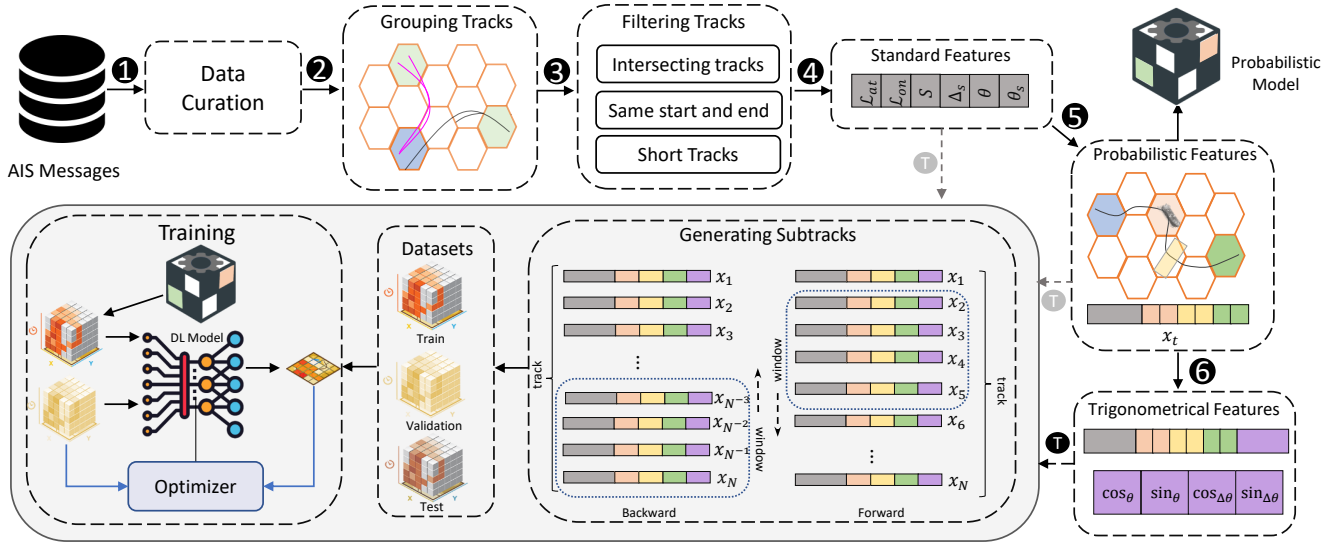


Figure 6. Visual representation of our pipeline. We start with a subset of AIS messages that cover the Gulf of St. Lawrence. After curating the data and separating messages by MMSI into tracks (**Step 1**), we then group the tracks by the pattern based on common start and end (**Step 2**). This means the dataset is divided into subsets with a balanced number of trajectories based on their unique patterns, and then the samples are weighted according to their population. All short tracks, self-intersecting tracks, and tracks having the same start and end port are removed (**Step 3**). From the basic positional attributes, we then calculate bearing, speed, and their deltas to form the *Standard Features* set (**Step 4**). This features set is then extended by adding *Probabilistic Features*, and for that, we consider the start and end of each track and the closest route polygon placed in the gulf, which is used for directing the vessel under the condition of having multiple paths (**Step 5**). These new features are used for the learning of the probabilistic model. We then add *Trigonometrical Features* for each message of tracks to extend the existing feature set (**Step 6**). For each track, using a forward and backward sliding window technique, we generate sub-sequences in contiguous temporal slices of ideally 3 hours of input and 12 hours of output data to construct training, validation, and testing datasets (**Step T**). After applying a temporal mini-batch training method, we optimize the neural network to identify the best subset of parameters that can closely forecast the samples in the training set. When training with probabilistic features, each sample is updated to have the additional engineered features coming from the probabilistic model before feeding to the neural network. This training process is repeated several times until there is no further improvement when testing the model on the validation-reserved data. The output is a trained network ready to be evaluated on the test dataset.

apart based on their timestamp. The data contains more than ten types of vessels; however, we only consider cargo and tanker vessels in our study due to the distinguishable nearly-linear movement behavior (**Step 1**). During this process, we consider the variations in vessel paths, aiming to reduce uncertainty in the later trajectory forecasting by segmenting voyages into individual end-to-end trajectories (**Step 2**). As a

result, a vessel's MMSI can be present in the dataset multiple times with different tracks (*i.e.*, trajectories). This segmentation is based on factors such as time, speed, and distance intervals between consecutive AIS messages. We keep only those segments that comply with the at least 13-hour period required for the tracks. This allows us to generate a refined dataset version that only includes segmented trajectories with end-to-end trip behavior, meaning feasible motion without major disturbances and unpredictable events. For the sake of conciseness, messages within a kilometer of the nearest port are discarded due to the high probability of the vessel being anchored. Similarly, trajectories originating and concluding at the same port, typically seen in fishing vessels, as well as tracks with self-intersecting trajectories, are also discarded (**Step 3**). At this point, we further discard tracks from the dataset if they represent moving patterns that are outliers and do not cope with mobility patterns widely present in the dataset of Cargo and Tanker vessels. We identify outlier tracks based on their connection with the grid-cells. If the number of tracks starting and ending in a particular pair of grid-cells is less than or equal to 5, we remove all those tracks. That is the case of trajectories potentially indicating vessels patrolling around marine protected areas that might have been mislabeled during the dataset collection. The resulting dataset has vessels grouped by their MMSI and divided by their type, with sets of segmented trajectories containing only the coordinates.

We reverse the trajectories and add them to the dataset as new trajectories to increase the sample size for the experiment. Based on the distance between the consecutive points previously interpolated every 10 minutes, we calculate the speed displacement of the vessel and its acceleration in knots per hour. We do the same to identify the bearing of the vessel and the rate of the change of the bearing in degrees (see Methods). This information is included in each AIS message of curated trajectories (**Step 4**). It forms the first set of features used in this research, known as *Standard Features*. Further, we split trajectories at points where the rate of change of the bearing varies by more than $\pm 45^\circ$. The output of this process is divided into sections for training, testing, and validation based on the vessel type and MMSI (**Step T**).

The standard feature set of the track is extended with the current grid-cell, route polygon, and last grid-cell centroids (**Step 5**). This extended feature set is called *Probabilistic Features*. Using the training dataset, we train the probabilistic model and, later, the deep-learning one. In such a stage, we identify common routes over the historical training data and their probable destinations. The existence of multiple routes between frequently traveled source and destination ports indicates the need for the creation of route polygons, which is further backed up by the analysis of vessel density maps. At the final stage of this process (**Step 6**), we extend the feature set with cartesian features. We now have both a refined and smaller dataset of *Standard Features* and the probabilistic models for expanding them into the *Probabilistic* and *Trigonometrical Features* proposed by this study. In the ablation study, either of the feature sets at **Step T** can be used to generate training, testing, and validation datasets. For example, **Step T** for the trigonometric feature set is enabled in Figure 6 whereas standard and probabilistic feature sets are grey-out.

Subsequently, we proceed toward neural network engineering and training. The dataset slices now go through a sliding window algorithm, which formats the data as required by the deep-learning model. Such an algorithm shapes the 1 to 3-hour input data into vectors of equal size, padding values whenever they

are missing. The output vectors always have 12 hours, and no padding is applied to them. The sliding window algorithm iterates over the temporal data every 30 minutes, processing 3 new messages at a time. We allow the last element in the training input vector to be present as the first element of the output vector (*i.e.*, overlap of 10 minutes) to enhance the continuity of the data and help the model perform better. The sliced windows from this process are then zero-one normalized and ready for use by the deep-learning model. At this stage, regardless of the feature set we will use, we expect the model to generate a pair of normalized coordinates in the range of $[0, 1]$ as output. These coordinates, when denormalized, should resemble the anticipated output of the vessel trajectory. Such models are trained on the same training data that was used to build the probabilistic model. The training continues until no improvement is seen on the validation-reserved dataset slice. Finally, the models are validated on the test dataset of reserved vessels. The training and validation are conducted simultaneously on tankers and cargo vessels. However, the final testing is performed separately so that we can account for the individual performance by vessel type.

Our experiments involve testing different sets of features and network architectures. Our contributions are on feature engineering and neural network modeling, which together can make complex long-term path decisions. We conducted experiments with three distinct sets of features and displayed the results of other neural network models in an ablation fashion. We covered comparisons with the literature and state-of-art, including simple RNNs^{51–53}, Bidirectional RNNs^{54–56}, CNNs/RNNs AutoEncoders^{57–59}, and combinations of those with and without the transformer-based attention mechanism, all of which have less than 1.5M trainable parameters. We chose not to test models that exceeded the threshold due to their large size and long training time requirements. As AIS is a type of streaming data, it requires models that can train and produce fast outputs. Our proposal suggests using smarter features in combination with simpler, well-tailored models. Additionally, in the context of the Gulf of St. Lawrence, there is not enough data and information available to justify the use of larger and deeper models. These models may not necessarily provide better results but will certainly require more resources and take longer sessions to train and refine.

Differently from the literature, our model uses parallel Convolutional Neural Networks (CNNs) to extract local and global features from input data through dilated convolutions. The CNNs' outputs are combined and processed by a Bidirectional Long Short-Term Memory (Bi-LSTM) with a Position-Aware Attention mechanism, efficiently encoding the temporal sequence, giving higher importance to later timesteps. The resulting latent space is then decoded through a second Bi-LSTM and multiple Dense layers, giving the final output as normalized latitude and longitude values. This end-to-end, customizable architecture achieves superior performance in predictive geospatial tasks, mainly when trained with the aid of probabilistic and trigonometrical features. So, to start this discussion, subsequently, we formalize our probabilistic model while using Table 1 to describe the symbols and notations used from hereinafter.

Probabilistic Features

A trajectory is a sequence of points representing the location of an object over time, and, in this paper, a trajectory τ is represented as an ordered sequence of t points in time, such as $\tau = \langle x_1, x_2, \dots, x_t \rangle$,

Table 1. Symbols and notations relevant for the probabilistic model formulation understanding.

Notation	Definition
τ	A trajectory — an ordered sequence of t points
x_t	A point in a trajectory at instant t , in format $\langle \mathcal{L}_{on}, \mathcal{L}_{at}, S, \Delta_S, \theta, \Delta_\theta \rangle$
\mathcal{L}_{on}	Longitude in degrees
\mathcal{L}_{at}	Latitude in degrees
S	Speed in nautical miles
Δ_S	The acceleration in nautical miles of the vessel
θ	Bearing in degrees
Δ_θ	The rate of change of the bearing in degrees
\mathbf{M}	Route probability matrix $\mathbf{M} \in \mathbb{R}^{c \times r \times z}$, where c is the number of grid-cells, r is the number of route-polygons and z is number of tracks from c passing through r
$\tilde{\mathbf{M}}$	Destination probability matrix $\tilde{\mathbf{M}} \in \mathbb{R}^{c \times c \times z}$, where c is the number of grid-cells and z is number of tracks passing through a given grid-cell
C	Set of all grid-cells $C = \{C_i\}_{i=1}^c$
D	Subset of destination grid-cells $D = \{D_j\}_{j=1}^d$ where $D \subseteq C$
T	Collection of trajectories $T = \{\tau_i\}_{i=1}^n$, where n is the number of trajectories
T_{C_i}	Subset of trajectories that have passed through a specific grid-cell C_i
T_{D_j}	Set of trajectories that ended up in D_j
S_{τ_i}	A tuple of motion statistics of track τ_i in format $\{\mathcal{L}_f, \mathcal{L}_e, \tilde{\theta}_g, \Psi_{\theta_g}\}$
\mathcal{L}_f	First AIS coordinates of track τ_i within a grid-cell C_i
\mathcal{L}_e	Last AIS coordinates of track τ_i within a grid-cell C_i
$\tilde{\theta}_g$	The median of the course values of vessel movements in a grid-cell
Ψ_{θ_g}	The Gaussian Kernel Density Estimation-based entropy of the bearing values
δ	Euclidian distance threshold for motion statistics, first quantile of all pre-computed distances
$\mathbf{I}(\cdot)$	Indicator function, outputs 1 if a trajectory satisfies the input conditions, else 0
E	Euclidian distance function, as defined in Equation 1
\mathcal{L}^R	Predicted route centroid coordinates, where $R \subseteq C$
\mathcal{L}^N	Current grid-cell's centroid coordinates, where $N \subseteq C$
\mathcal{L}^D	Predicted destination grid-cell's centroid coordinates, where $D \subseteq C$

where a point $x_t \in \tau$ at time t is also an ordered sequence of features from the AIS message such as $x_t = \langle \mathcal{L}_{on}, \mathcal{L}_{at}, S, \Delta_S, \theta, \Delta_\theta \rangle$; where \mathcal{L}_{on} is the longitude, \mathcal{L}_{at} the latitude, S the speed in nautical miles, θ the bearing in degrees, Δ_S the acceleration in nautical miles, and Δ_θ the rate of change of the bearing in degrees. We refer to the set of values in x_t of each AIS message as *Standard Features*. The speed, bearing,

and deltas can be mathematically calculated using sequences of coordinates (see Methods).

Our approach involves probabilistic modeling where we consider a 310-cell grid that overlays the Gulf of St. Lawrence and six-year historical AIS data to create a Route Probability Matrix $\mathbf{M} \in \mathbb{R}^{c \times r \times z}$ and a Destination Probability Matrix $\tilde{\mathbf{M}} \in \mathbb{R}^{c \times c \times z}$. Here, c represents the number of cells, r is the number of possible routes (route polygons), and z is the number of tracks passing through a grid-cell or route polygon. Through those, we aim to generate a probable route and destination that can be used as features for deep-learning models to forecast vessels' trajectories. It is important to note that our probabilistic model does not predict the next grid-cell of the vessel during the vessel displacement in the trajectory. Instead, it predicts the probable long-term decisions that vessels will make. To this end, we have a collection of trajectories T , another of grid-cells C , and a last one of destination grid-cells D . We use T_{C_i} to refer to a subset of trajectories that have passed through a particular grid-cell C_i and T_{D_j} to represent the set of trajectories that ended up in D_j , $i \neq j$. For a simple conditional probability formulation where z , the individual tracks interacting with the grid-cells, is not taken into account, one could populate \mathbf{M}_{ij} with the conditional probability of a trajectory between C_i and a route polygon R_k as $\mathbb{P}(R_k|C_i) = |T_{R_k} \cap T_{C_i}| \div |T_{C_i}|$ and populate $\tilde{\mathbf{M}}_{ij}$ with the one between C_i and a destination grid-cell D_j as $\mathbb{P}(D_j|C_i) = |T_{D_j} \cap T_{C_i}| \div |T_{C_i}|$.

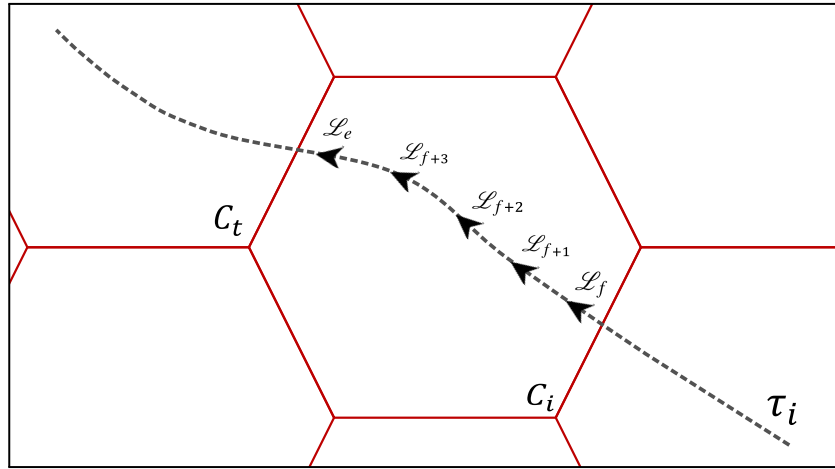


Figure 7. An example of AIS messages of a vessel inside a grid-cell

Unfortunately, conditional probabilities alone cannot accurately describe the transition between grid-cells. This would lead to a bias towards shipping routes with higher vessel traffic over time. Moreover, assuming an equal distance between all grid-cells neglects the importance of the vessel course and its distance (from the last AIS message location) to the nearest route polygon. Because of that, we consider the relationship of the vessel location with the route polygon. We do so by accounting for the trajectory path coming from T_{C_i} and the direction of the movement while passing through C_i , as depicted in Figure 7. Such information is stored on the last axis of our probability matrices $\mathbf{M} / \tilde{\mathbf{M}}$, previously referred to as z , and hereinafter named after *motion statistics*. The motion statistics for each track $\tau_i \in T_{C_i}$ consist of four values, which are represented by $S_{\tau_i} = \{L_f, L_e, \tilde{\theta}_g, \Psi_{\theta_g}\}$. Within C_i , L_f and L_e represent the first

and last pair of coordinates, respectively, of τ_i — *e.g.*, $\mathcal{L}_f = \langle \mathcal{L}_{lon}^f, \mathcal{L}_{lat}^f \rangle$; $\tilde{\theta}_g$ is the median of the course values; and, Ψ_{θ_g} is the Gaussian Kernel Density Estimation-based entropy of the course values within the messages inside C_i . Each S_{τ_i} is associated with a route polygon $S_{\tau_i} \rightarrow R_k$ or possible destination $S_{\tau_i} \rightarrow D_{\tau_i}$, in which, each motion statistic is computed to define feasible transitions between routes and destination.

To refine the probabilities, we compare the distances of motion statistics from historical tracks stored on the route polygons and destination grid-cells. Let us take the example of a new track, denoted by τ_n , that spans three cells in C , with C_i representing the vessel's current location, and $S_{\tau_n}^{C_i}$ the motion statistics. For each $S_{\tau_i}^{C_i}$ within T_{C_i} , we calculate the Euclidean distance between $S_{\tau_n}^{C_i}$ and $S_{\tau_i}^{C_i}$ using the following equation:

$$Euclidean(S_{\tau_n}^{C_i}, S_{\tau_i}^{C_i}) = \sqrt{(\mathcal{L}_f^{\tau_n} - \mathcal{L}_f^{\tau_i})^2 + (\mathcal{L}_e^{\tau_n} - \mathcal{L}_e^{\tau_i})^2 + (\tilde{\theta}_g^{\tau_n} - \tilde{\theta}_g^{\tau_i})^2 + (\Psi_{\theta_g}^{\tau_n} - \Psi_{\theta_g}^{\tau_i})^2} \quad (1)$$

where \mathcal{L}_f and \mathcal{L}_e represent starting and ending coordinates; and, $\tilde{\theta}_g$ and Ψ_{θ_g} refer to the median and entropy of bearing values, respectively. The distance, in this case, is calculated between the current track τ_n and each historical track τ_i inside grid-cell C_i . In this calculation, every value in S_{τ} is normalized between the range $[0, 1]$, which ensures that all features have equal influence on the distance measure. The route polygons or grid-cells demonstrating the lower Euclidean distance relationship are considered the most similar and indicate the most probable route a vessel will take or the destination a vessel will reach.

We can summarize the conditional probabilistic process using Figure 8 as an example. The figure depicts a vessel moving from point A to C, with a decision point at the segment between B and C. At this decision point, there are two possible paths, each of which interacts with a different route polygon (R_i and

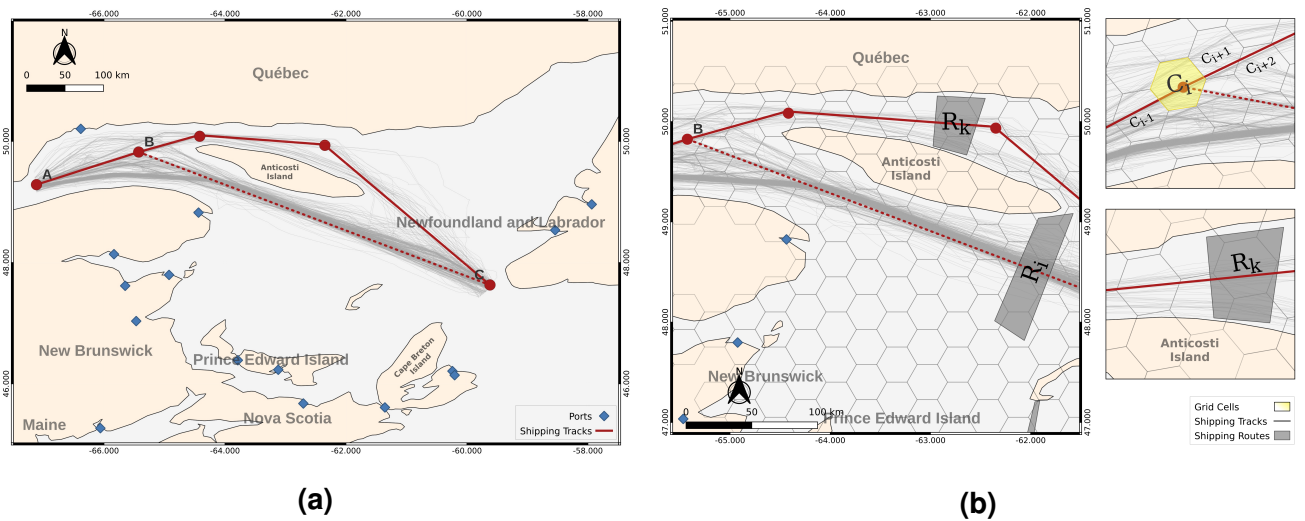


Figure 8. The image (a) displays a density map depicting two routes from a starting point A towards the endpoint C. In image (b), the region has been divided into hexagonal grid-cells of 0.3° using *ESPG:4269* projection, where a grid-cells are referred to as C_i and possible routes as R_i and R_k . The solid red line shows the probable movement of a vessel between B and C, and the dashed line shows a less probable one.

R_k). The solid red line represents the most probable path, while the dashed line shows the least probable path. To define a probable route, we need to consider the location of the route polygon (R_k or R_i), the vessel's current location (C_i), and the motion statistics obtained from historical tracks (S_τ). We can define the probability function for the route definition using the following equation:

$$\mathbb{P}(R_k|C_i, S_\tau) = \xi \times \frac{\sum_{x \in T} \mathbf{I}(S_{\tau_i} = S_\tau \wedge x_t \in R_k \wedge E(S_{\tau_n}, S_{t_i}) \leq \delta \wedge \exists(x_t) \in C_i)}{\sum_{x \in T} \mathbf{I}(S_{\tau_i} = S_\tau \wedge E(S_{\tau_n}, S_{t_i}) \leq \delta \wedge \exists(x_t) \in C_i)}; \quad (2)$$

although the destination D_j is already known in Figure 8 as C, we can formalize the probabilistic function for the destination forecasting, with respect to the route polygon R_k , using the equation bellow:

$$\mathbb{P}(D_j|C_i, R_k, S_\tau) = \xi \times \frac{\sum_{x \in T} \mathbf{I}(S_{\tau_i} = S_\tau \wedge x_t \in D_j \wedge E(S_{\tau_n}, S_{t_i}) \leq \delta \wedge \exists(x_t) \in C_i \wedge \exists(x_t) \in R_k)}{\sum_{x \in T} \mathbf{I}(S_{\tau_i} = S_\tau \wedge E(S_{\tau_n}, S_{t_i}) \leq \delta \wedge \exists(x_t) \in C_i \wedge \exists(x_t) \in R_k)}; \quad (3)$$

in cases where the route polygons are known not to interact with the historical trajectories, such as in the case of Figure 4c, we can simplify the conditional probabilistic destination model from above as follows:

$$\mathbb{P}(D_j|C_i, S_\tau) = \xi \times \frac{\sum_{x \in T} \mathbf{I}(S_{\tau_i} = S_\tau \wedge x_t \in D_j \wedge E(S_{\tau_n}, S_{t_i}) \leq \delta \wedge \exists(x_t) \in C_i)}{\sum_{x \in T} \mathbf{I}(S_{\tau_i} = S_\tau \wedge E(S_{\tau_n}, S_{t_i}) \leq \delta \wedge \exists(x_t) \in C_i)}; \quad (4)$$

the Equations 2, 3, and 4 take into account all the trajectories in the dataset, T . The selection of appropriate trajectories in the numerator and denominator is guided by the indicator function $\mathbf{I}(\cdot)$, which outputs 1 (*i.e.*, True) if a trajectory satisfies certain conditions. For Equation 2, which calculates the route-probability, a trajectory is selected if it meets four criteria: **(a)** the historical motion statistics is equivalent to the current trajectory, **(b)** a point within the trajectory falls into the route polygon R_k , **(c)** the Euclidean distance E to the current vessel's motion statistics is less than a threshold δ — the first quantile value of all pre-computed distances between historical motion statistics (see Algorithm 1) —, **(d)** there exists at least one point from both the current cell C_i and the route polygon R_k in this trajectory. In Equation 3, which considers the destination probability with the interacting route polygon R_k , the criteria are the same as in Equation 2, but with a change in **(b)**: a point within the trajectory falls into the destination cell D_j , instead of the route polygon. For Equation 4, which calculates destination probability without considering an interacting route polygon, the criteria are much the same as 2 and 3, but it no longer requires a point in the trajectory to fall into the route polygon R_k . For the denominators in all three equations, the trajectories are selected if they contain at least one point in the current cell C_i and have motion statistics similar to the current trajectory. The final probability for these equations is based on the multiplication of the resulting fraction with the similarity score based on the motion statistics values, given by $\xi = (1 - E(S_{\tau_n}, S_{t_i}))$.

The proposed conditional probabilistic models are then used to enhance vessel trajectory data by generating revised tracks with additional features. These are referred to as *Probabilistic Features* and include the predicted routes and destination for each vessel trajectory. The new features come from

converting the transition probabilities into cell-grid centroids that are later appended to the AIS messages within the vessel track. For example, a point x_t at time t from a trajectory $x \in \tau$ is now known to be of shape $x_t = \langle \mathcal{L}_{on}, \mathcal{L}_{at}, S, \Delta_S, \theta, \Delta_\theta, \mathcal{L}_{on}^R, \mathcal{L}_{at}^R, \mathcal{L}_{on}^N, \mathcal{L}_{at}^N, \mathcal{L}_{on}^D, \mathcal{L}_{at}^D \rangle$. Here, \mathcal{L}^R indicates the coordinates of the route polygon if the track is predicted to intersect with at least one of the known routes; \mathcal{L}^N indicates the coordinates of the grid-cell where the vessel currently lies; and, \mathcal{L}^D indicates the coordinates of the destination grid-cell of the track; where, C represents all grid-cells, $R \subseteq C$, $N \subseteq C$ and $D \subseteq C$.

Defining the final set of features relies on conditions that depend on the number of routes identified in the dataset and the intersection of the trajectories of interest with the route polygons. In this sense, defining \mathcal{L}^D , which is the same for an entire track, depends on the following equation:

$$\mathbb{P}(D_j|C_i, S_\tau) = \begin{cases} \mathbb{P}(D_j|C_i, R_k, S_\tau) & \text{if } \max_k [\mathbb{P}(R_k|C_i, S_\tau)] > 0, \\ \mathbb{P}(D_j|C_i, S_\tau) & \text{otherwise.} \end{cases} \quad (5)$$

where the destination of a track is conditional to the existence of a route polygon that interacts with the trajectory or is independent of it otherwise; knowing that C_i is where the vessel lies, D_j is the possible destination within any of the 310 cells, and R_k is one of the 4 route polygons previously identified in the gulf. Differently, defining \mathcal{L}^R , which is also shared with the entire track, depends on the next equation:

$$\mathbb{P}(R|C_i, S_\tau) = \begin{cases} \max_k [\mathbb{P}(R_k|C_i, S_\tau)] & \text{if } \max_k [\mathbb{P}(R_k|C_i, S_\tau)] > 0, \\ \max_j [\mathbb{P}(D_j|C_i, S_\tau)] & \text{otherwise.} \end{cases} \quad (6)$$

such a case takes into consideration that not all tracks interact with a known route polygon, and whenever this happens, the centroid of the route polygon \mathcal{L}^R is replaced by the centroid of the most probable destination \mathcal{L}^D among the grid-cell in the gulf so to increasing the robustness of the probabilistic model.

Trigonometrical Transformations

Predictive modeling for trajectory data presents challenges in representing geospatial data when measured in degrees, such as for longitude, latitude, and bearing. Traditional Recurrent Neural Networks (RNNs), including Long Short-Term Memory (LSTM) networks, may not be able to properly interpret these variables' cyclical and cardinal nature when directly used in learning, even if $[0, 1]$ normalized. This can result in artificially induced discontinuities and misinterpreted spatial relationships within the dataset. That is because the degree space is not contiguous with the physical space, as is the case of the Cartesian plane.

To better handle degree-based data, it is helpful to use transformations that maintain their inherent cyclical relationships. When dealing with longitude and latitude values, we can project them onto a unit sphere (*i.e.*, radius one). This mapping method transforms the data onto a three-dimensional surface while encoding its geodesic similarities into a nearly Cartesian space using the following sequence of equations:

$$\begin{aligned} \alpha &= \cos(\mathcal{L}_{on}) \times \cos(\mathcal{L}_{at}) \\ \beta &= \sin(\mathcal{L}_{on}) \times \cos(\mathcal{L}_{at}) \\ \gamma &= \sin(\mathcal{L}_{at}) \end{aligned} \quad (7)$$

where \mathcal{L}_{on} is the longitude and \mathcal{L}_{at} is the latitude, and $\alpha, \beta, \gamma \in [0, 1]$. This type of transformation is designed to maintain the spatial relationships between points on the Earth's surface, ensuring that nearby points remain adjacent in the transformed representation. However, it becomes inaccurate when dealing with data that is located too close to the Earth's poles, such as in the Arctic Ocean. Unlike coordinates, bearing values cannot be projected directly onto a Cartesian space. However, they can be transformed using cosine and sine functions, which enable a sinusoidal representation of the data. This representation helps in understanding the continuity of values in space as the vessel moves and is achieved as follows:

$$\begin{aligned}\cos_{\theta} &= \cos\left(2\pi \times (\theta \div 360)\right) \\ \sin_{\theta} &= \sin\left(2\pi \times (\theta \div 360)\right)\end{aligned}\quad (8)$$

For speed, valued in nautical miles, applying the logarithmic transformation can be effective, especially when dealing with data spanned across multiple orders of magnitude. This can ensure that larger-scale patterns do not overly influence the model, allowing local trends to play a part in the decision-making process. This can be achieved with the equation $S' = \log(1 + |S|)$, where S' is the transformed and S is the original speed. Through these sets of transformations, the earlier point x at time t from a trajectory τ become $x_t = \langle \mathcal{L}_{on}, \mathcal{L}_{at}, \alpha, \beta, \gamma, S, \Delta_S, \theta, \Delta_{\theta}, S', \Delta_{S'}, \cos_{\theta}, \sin_{\theta}, \cos_{\Delta_{\theta}}, \sin_{\Delta_{\theta}}, \mathcal{L}_{on}^R, \mathcal{L}_{at}^R, \alpha^R, \beta^R, \gamma^R, \mathcal{L}_{on}^N, \mathcal{L}_{at}^N, \alpha^N, \beta^N, \gamma^N, \mathcal{L}_{on}^D, \mathcal{L}_{at}^D, \alpha^D, \beta^D, \gamma^D \rangle$. This final representation includes *Standard*, *Probabilistic*, and *Trigono-*

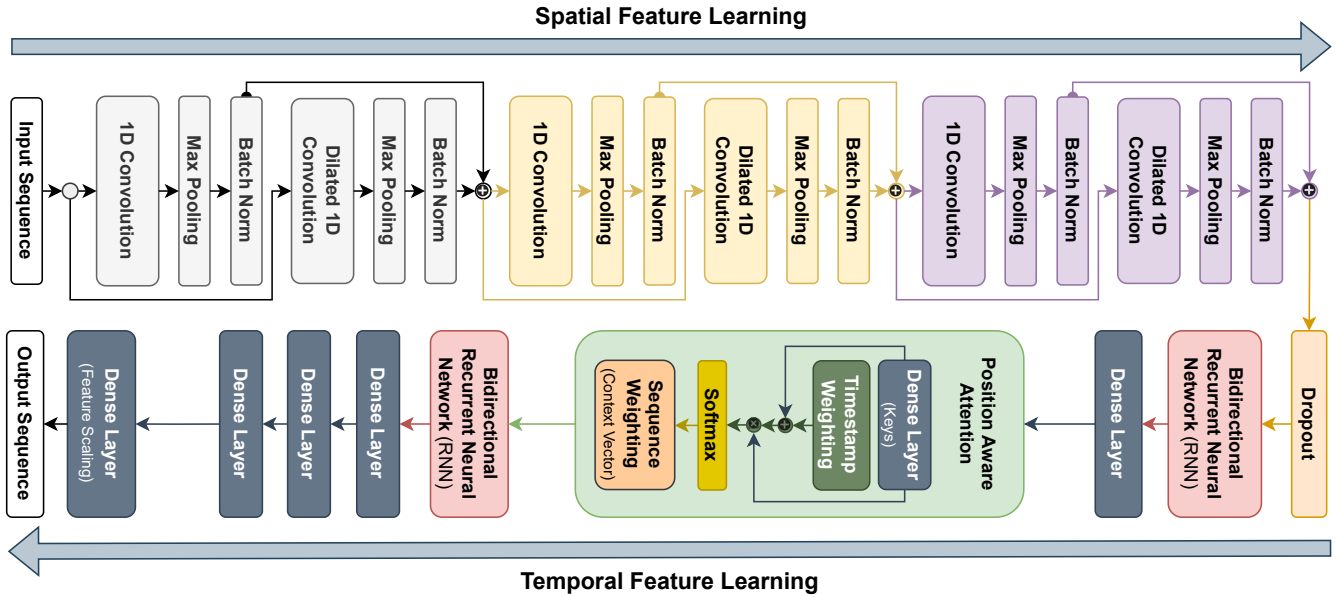


Figure 9. The proposed deep-learning model uses parallel convolutions and a sequential stack of convolution blocks to capture short and long-term spatial features. The extracted features are passed through a dropout layer and a Bi-LSTM with a fully connected layer. The Position-Aware Attention mechanism enhances the importance of later timestamps. The final encoded latent space undergoes a Bi-LSTM decoding phase and a multi-layer fully connected network to produce normalized coordinates.

metrical Features. It provides an enriched input dataset for the deep-learning model tailored for trajectory forecasting, facilitating its understanding of complex spatial and temporal patterns of the trajectories. With all feature sets properly defined, we move forward with the formalization of the deep-learning model (see

Table 2. Symbols and notations relevant for the deep-learning model formulation understanding.

Notation	Definition
b	Batch size of the input tensor
w	Window size of the input, which represents the number of timestamps
v	Number of features in each input timestamp
f	Size of convolution filters
s	Stride of convolution layers
m	Number of filters in convolution layers
\mathbf{x}	Input tensor to the model, of shape $\mathbb{R}^{b \times w \times v}$
\mathbf{W}	Representation of the weights of the model layers
\mathbf{b}	Representation of the bias parameters of the model layers
\star	Cross-correlation operator used by single-dimensional convolutions
\tilde{w}	Reduced size of window after convolution
ϵ	Small constant to avoid division by zero
$\mu_b^d, (\sigma_b^d)^2$	Mean and variance for each filter d within batch b in batch normalization
γ^d, β^d	Scaling and shifting parameters for each filter d in batch normalization
h	Size of max pooling filter
d	Feature dimensions – changes with each iteration through layers
ϑ	Dilation factor for kernel expansion in dilated convolutions
$\mathbf{C}, \tilde{\mathbf{C}}$	Cell state and candidate cell state of the Bi-LSTM
\mathbf{i}, \mathbf{f}	Input gate and forget gate of the Bi-LSTM
\mathbf{o}, \mathbf{h}	Output gate and hidden state of the Bi-LSTM
$\sigma(\cdot)$	Sigmoid activation function of the Bi-LSTM
$\phi(\cdot)$	Activation function used in the model (<i>i.e.</i> , ReLU)
\mathbf{A}	Attention weights for Position-Aware Attention mechanism
\mathbf{E}	Position-Aware context vector of shape $\mathbb{R}^{b \times z \times d}$
\otimes	Tensor repeating and concatenation operator
ω	Time factor for establishing a focal point in attention mechanism
z	Window size of the output, which represents the number of output timestamps
$\Xi(\cdot)$	Re-scaling function for coordinate values generation
\mathbf{y}	Final output tensor representing latitude and longitude, of shape $\mathbb{R}^{b \times z \times 2}$

Figure 9), which is based on Table 2 for describing the symbols and notations used from hereinafter.

Neural Network Architecture

Giving an input tensor $\mathbf{x} \in \mathbb{R}^{b \times w \times v}$, where b denotes the batch size, w denotes the window size of the input vectors, and v denotes the number of features. Our model begins by executing single-dimensional parallel convolutions. Essentially, we slide a filter (also known as a kernel) of size f across each window element and calculate the dot product across all features with a stride of s for each filter m . This way, we process the input tensor to extract spatial features that will be used in subsequent model layers.

$$\mathbf{x}_{b,i,m} = \sum_{j=1}^f \sum_{n=1}^v \mathbf{x}_{b,(i+(s \times (j-1))),n} \cdot \mathbf{W}_{m,j,n} \equiv \mathbf{x}_{b,i} \star \mathbf{W}_m \quad (9)$$

Based on the filter size f and stride s , we follow this operation for each window element to yield an output tensor $\mathbf{x} \in \mathbb{R}^{b \times \tilde{w} \times m}$, where \tilde{w} represents the new window size and m denotes kernel size. The cross-correlation \star operation represents an equivalent of this convolution. The convolutional layers play a crucial role in extracting spatial features of the input trajectories, especially for long-term trajectory forecasting. These layers are particularly helpful when the input data is limited to short-term data. They can learn spatial patterns like curves and slight course changes based on historical data, but they tend to overfit the input data and can only learn patterns that fit their kernel size.

Subsequently, $\mathbf{x} \in \mathbb{R}^{b \times \tilde{w} \times m}$ goes through batch normalization to fit the values of the resulting tensor into a standard scale. This is followed by a max-pooling operation, and the two processes are defined as:

$$\mathbf{x}_{b,i,d} = \mathbf{max} \left(\frac{\mathbf{x}_{b,p,d} - \mu_b^d}{\sqrt{(\sigma_b^d)^2 + \epsilon}} \cdot \gamma^d + \beta^d \right) \quad \forall p \in [i, i+h-1] \quad (10)$$

For each filter, d and batch b , a window of size h is defined on the feature map starting at position i , with the condition that $i+h-1 \leq \tilde{w}$. The filter-wise mean μ_b^d and variance $(\sigma_b^d)^2$ are calculated for batch b , along with specific scaling γ^d and shifting β^d parameters. Next, the max pooling operation is performed over the window, extracting the maximum value of p . The resulting value is assigned to $\mathbf{x}_{b,i,d}$, which becomes the feature map for the given window of filter index d . Due to working with parallel convolutions that involve different kernel sizes, it is necessary to use a combination of techniques to ensure consistent tensor dimensions. We use batch normalization and max-pooling to scale down the tensor dimensions into shared tensor dimensions with scaled values, which can be merged later. This approach guarantees that the branches can be combined seamlessly without stability issues during the training.

As mentioned, single-dimensional CNNs can only learn spatial features within their kernel size. We employ parallel convolutions in residual blocks to capture both short-term and long-term spatial features simultaneously. This is achieved through dilated convolutional layers, which expand the kernel size by a factor of ϑ and enable it to capture extended spatial features from the input data. Both convolutional

branches in a block are trained together, but they work independently on copies of the input data such that they are not affected by each other. To perform dilated convolution, we modify Equation 9 as follows:

$$\mathbf{x}_{b,i,m} = \sum_{j=1}^f \sum_{n=1}^v \mathbf{x}_{b,(i+(s \times \vartheta \times (j-1))),n} \cdot \mathbf{W}_{m,j,n} \equiv \mathbf{x}_{b,(i+\vartheta)} \star \mathbf{W}_m \quad (11)$$

where j stands for the filter index, and $\vartheta \times (j-1)$ is the expansion of the kernel due to the dilation rate ϑ . The resulting output of the branches, given by Equation 10, is then combined into a single tensor as such:

$$\mathbf{x}_{b,i,m} = \mathbf{x}_{b,i,m}^T + \mathbf{x}_{b,i,m}^D \quad (12)$$

we use T and D to indicate the results obtained from traditional and dilated convolutions.

The series of mathematical operations that end in Equation 12, as shown in Figure 9, is repeated three times, each time with different parameters. At this point, \tilde{w} and m have dimensions according to the hyperparameters of the convolution block (see Methods). This stack allows us to extract more precise long and short-term spatial features from the input data at each process step. The parallel CNNs and the sequential blocks work simultaneously to produce a refined output of spatial features that is then sent to the next block for further processing, minimizing further the overall error for the forecasting task.

The subsequent part is where the network learns the temporal features from the input data. It starts with a dropout layer to prevent overfitting from the spatial feature data. The dropout layer comprises a binary mask of shape $\mathbb{R}^{b \times \tilde{w} \times m}$, where each element has a value of 1 with probability p and a value of 0 with probability $1 - p$, which is element-wise multiplied with the input data to generate the output. Such output is forwarded to a Bidirectional Long-Short Term Memory (Bi-LSTM) network, which takes $\mathbf{x} \in \mathbb{R}^{b \times \tilde{w} \times m}$ as input and produces the hidden state $\mathbf{h}_{b,i,r} \in \mathbb{R}^{b \times \tilde{w} \times r}$ for each time step $i \leq \tilde{w}$, where r is the dimension of the LSTM inner weights. The Bi-LSTM equations can be formulated as follows:

$$\begin{aligned} \mathbf{i}_{b,i,r} &= \sigma \left(\mathbf{W}_i \cdot \left[\mathbf{h}_{b,(i-1),r}, \mathbf{x}_{b,i,m} \right] + \mathbf{b}_i \right) \\ \mathbf{f}_{b,i,r} &= \sigma \left(\mathbf{W}_f \cdot \left[\mathbf{h}_{b,(i-1),r}, \mathbf{x}_{b,i,m} \right] + \mathbf{b}_f \right) \\ \tilde{\mathbf{C}}_{b,i,r} &= \tanh \left(\mathbf{W}_C \cdot \left[\mathbf{h}_{b,(i-1),r}, \mathbf{x}_{b,i,m} \right] + \mathbf{b}_C \right) \\ \mathbf{o}_{b,i,r} &= \sigma \left(\mathbf{W}_o \cdot \left[\mathbf{h}_{b,(i-1),r}, \mathbf{x}_{b,i,m} \right] + \mathbf{b}_o \right) \\ \mathbf{C}_{b,i,r} &= \mathbf{f}_{b,i,r} \cdot \mathbf{C}_{b,(i-1),r} + \mathbf{i}_{b,i,r} \cdot \tilde{\mathbf{C}}_{b,i,r} \\ \mathbf{h}_{b,i,r} &= \mathbf{o}_{b,i,r} \cdot \tanh \left(\mathbf{C}_{b,i,r} \right) \\ \mathbf{x}_{b,i,r} &= \phi \left(\mathbf{W}_d \cdot \left[\mathbf{h}_{b,i,r}^{\rightarrow} + \mathbf{h}_{b,i,r}^{\leftarrow} \right] + \mathbf{b}_d \right) \end{aligned} \quad (13)$$

where σ is the sigmoid function, \tanh is the hyperbolic tangent function, $[\mathbf{h}_{b,(i-1),r}, \mathbf{x}_{b,i,m}]$ is the concatenation of the previous hidden state with the i -th element of the input. \mathbf{i} , \mathbf{f} , $\tilde{\mathbf{C}}$, \mathbf{o} , \mathbf{C} , and \mathbf{h} represent the input gate, forget gate, candidate cell state, output gate, cell state, and hidden state, respectively. $\mathbf{x}_{b,i,r}$

is the output of the process, where \mathbf{W}_d and \mathbf{b}_d is the weight and bias for the dense layer after the Bi-LSTM and ϕ is the activation function. Because Bi-LSTMs compute the hidden states in the forward $\mathbf{h}_{b,i,r}^{\rightarrow}$ and backward $\mathbf{h}_{b,i,r}^{\leftarrow}$ direction, the double output is merged before going through the fully-connected layer.

The next step of this process is to have the output of the fully connected layer go through the attention mechanism. As previously explained, due to working with sequences in which the order is essential, paying greater attention to later timestamps is more critical than early timestamps in the sequence. As such, we use a Position-Aware Attention mechanism that we propose for this use case, a further contribution of this paper. Given the input tensor $\mathbf{x}_{b,i,r}$, where $\mathbf{x} \in \mathbb{R}^{b \times \tilde{w} \times r}$, our model follows as:

$$\begin{aligned} \mathbf{K}_{b,i,r} &= \mathbf{x}_{b,i,r} \cdot \mathbf{W}_{b,i,r} + \mathbf{b}_{b,i,r} \\ \mathbf{S}_{b,i,r} &= \mathbf{K}_{b,i,r} \cdot \left(\mathbf{K}_{b,i,r} + (\omega \cdot (i \% w)) \right) \\ \mathbf{A}_{b,i,r} &= \text{softmax}(\mathbf{S}_{b,i,r}) \\ \mathbf{E}_{b,z,r} &= \left(\sum_{i=1}^w \mathbf{A}_{b,i,r} \cdot \mathbf{x}_{b,i,r} \right) \otimes \mathbf{1}_z \end{aligned} \quad (14)$$

In Equation 14, the attention keys are denoted by $\mathbf{K}_{b,i,m} \in \mathbb{R}^{b \times w \times d}$; and, to establish the focal point of attention, we compute a monotonically increasing score in respect to the index of the input tensor i and the time factor ω . We apply the dot product operation on the temporal-scaled samples to get the intermediate scores $\mathbf{S}_{b,i,r}$, followed by a *softmax* function to get the attention weights $\mathbf{A}_{b,i,r}$. Finally, we calculate the context vector $\mathbf{E}_{b,r}$ by performing a weighted summation of input vectors with the attention weights along with the temporal axis i . The context vector is then repeated z times to produce the encoded latent space representation $\mathbf{E}_{b,z,r}$ that will be decoded in the following by the subsequent layers of the model.

After the attention mechanism output (*i.e.*, context vector) has been created, it needs to be decoded to produce meaningful positional results. That is because, at this point, all the timestamps have the same value. The output of the attention mechanism is fed into a new Bi-LSTM with a similar formulation as in Equation 13. The difference in the decoding part is that the hidden states $\tilde{\mathbf{h}}_{b,z,r} \in \mathbb{R}^{b \times z \times \tilde{r}}$ of the Bi-LSTM goes through three fully connected layers instead of one, each of which can be represented as:

$$\mathbf{x}_{b,z,r}^k = \phi^k \left(\mathbf{W}_d^k \cdot \tilde{\mathbf{h}}_{b,z,r} + \mathbf{b}_d^k \right) \quad (15)$$

where ϕ^k is the activation function, \mathbf{W}_d^k and \mathbf{b}_d^k are the weight matrix and the bias for the k^{th} fully connected layer, respectively. $\mathbf{x}_{b,z,d}^k$ is the output of the k^{th} fully connected layer, where $k = 1, 2, 3$, z is the timestamps in the temporal axis, and d the transformed feature dimensions matching the size of the weights of the last fully connected layer. To produce the final set of forecasted coordinates, $\mathbf{x}_{b,z,r}^3$, needs to undergo a last transformation to reduce the axis d into a fixed size of 2, representing the longitude and latitude values:

$$\mathbf{y}_{b,z,\tilde{d}} = \Xi \left(\mathbf{W}_o \cdot \mathbf{x}_{b,z,d}^3 + \mathbf{b}_o \right) \quad (16)$$

where $\mathbf{y}_{b,i,\tilde{d}} \in \mathbb{R}^{b \times z \times 2}$ and Ξ is a custom re-scaling out function that can map the raw output values defined in $[0, 1]$ into the valid range of latitude $[-90, 90]$ and longitude $[-180, 180]$ coordinate values.

Results

The evaluation of results begins with the probabilistic features, which constitute the foundation of our proposal and the main catalyst for improved decision-making using neural networks in the task of multi-path long-term vessel trajectory forecasting. The probability model is trained on the same dataset that will be later used to train the deep-learning model. The crucial difference is that the deep-learning model's success hinges on the probabilistic model's successful implementation. The probabilistic model is responsible for feature engineering, while the deep-learning model focuses on trajectory forecasting based on the vessel position and its relevant probabilistic features. This means that when the deep-learning model has access to data regarding the vessel's intended route and destination, it can significantly decrease the uncertainty in trajectory forecasting, leading to better performance for the trajectory forecasting pipeline.

In the training phase of the model, we input ground-truth data regarding the routes and destinations of trajectories. The model uses this information to create transition probability matrices for routes and destinations. As the model is probabilistic in nature, it does not memorize the training data. Instead, it retains movement statistics based on their relation to grid cells. Applying the model to its training set data does not result in overfitting. This is because the model's probabilistic relationships are formed based on a general set of rules and decisions, which may only partially capture unique patterns in the training data. This results in uncertainty within the probabilities but does not compromise the accuracy of the model's results and decisions, as this is expected and can be managed within the learning framework.

We handle this uncertainty by deliberately not using the ground-truth route and destination data to train the deep-learning models. Instead, we apply the results from the probabilistic model to all further learning. In doing so, all subsequent learning about routes and destinations incorporates a degree of controlled uncertainty. This controlled uncertainty is directly proportional to the accuracy of the probabilistic model, creating a dynamic balance. Consequently, this approach mitigates the risk of the deep-learning model failing when the probabilistic model does. Sharing the responsibility of route and destination prediction across the two models makes the overall system more resilient. This strategy is particularly beneficial when dealing with streaming AIS data in real-time decision-making scenarios. Subsequent performance evaluations of the probability model across all data segments, for both training and testing datasets, are presented in Table 3. Further details about these metrics can be found in the Methods section.

The overperformance observed in the training datasets — especially in forecasting the destinations of the trajectories (scoring 89% and 87% F1 Score for cargo and tanker vessels, respectively) — are expected outcomes. Forecasting routes in both cases also yield reasonable results, achieving 80% and 82%. More impressively, when utilizing the test data — entirely unseen for the model — the outcome for route forecasting exceeded those observed during the training phase, scoring 81% and 87% for cargo and tanker vessels, respectively. However, regarding destination forecasting, we see a consistent decrease in performance, with the scores dropping to 75% and 74%, respectively. The observed performance difference between the training and testing datasets is an expected behavior. Even considering these

Probabilistic Model Results				
Test Type	Coordinate Type	Precision (%)	Recall (%)	F1 Score (%)
Cargo Test	Route	83.13	83.16	81.19
	Destination	75.28	79.09	75.85
Tanker Test	Route	86.89	89.92	87.84
	Destination	74.85	77.12	74.90
Cargo Train	Route	81.69	83.25	80.43
	Destination	89.51	89.72	89.02
Tanker Train	Route	83.43	84.29	82.31
	Destination	88.64	87.95	87.48

Table 3. Performance of the probabilistic model in forecasting a vessel’s route and destination.

variations, the results obtained are consistent, advocating for the effectiveness of the probabilistic model.

To evaluate the features’ performance in the deep learning model, we conducted experiments that compared all three sets of features by gradually removing parts of the network and observing the results. This ablation approach allowed us to assess the impact of each feature set on different neural network architectures. In this context, each model was tested with equal rigor over the *Default*, *Probabilistic*, and *Trigonometric Feature* sets, denoted as **A1/B1**, **A2/B2**, and **A3/B3**, respectively. We conducted a series of tests on five different model versions, which we labeled as **C1** through **C5**. The details of the tests can be found in Tables 4 and 5. **C1** represents our proposed model with all its layers included, while **C2** is the same model but without the parallel convolutions. On the other hand, **C3** is the proposed model without the attention mechanism, and **C4** is the model without both the parallel convolutions and the attention mechanism. Finally, **C5** refers to the model that uses simple unidirectional recurrent networks exclusively.

Our first noteworthy observation lies in the slight numerical variation in the R^2 Score across different experiments, as shown in Tables 4 and 5. This trend can be attributed to the nature of the data and the geographic traits of the Gulf of St. Lawrence region, which is an area with well-defined shipping lanes where most cargo and tanker vessels exhibit linear travel behavior with minimal or zero variations within the segments used to train our deep-learning model. Simultaneously, this pattern provides insights into the performance benefits of using probabilistic and trigonometrical features compared to the default ones. This is particularly noticeable when evaluating the 25th, 50th, and 75th percentile values. For cargo vessels, as presented in Table 4, we observe variation between 2 to 4 km for the 25th, 6 to 8 for the 50th, and 14 to 16 km for the 75th percentile across the default features. Although these error margins somewhat increase with using probabilistic features, they considerably decrease with the integration of trigonometrical ones. This indicates that the trigonometrical features can better predict the vessel route than the other ones.

Turning to tanker vessels, as shown in Table 5, we find that these models outperform cargo vessels, reflected by lower mean and standard deviation errors. However, percentile errors remain similar, generally

<i>Default Features</i>					<i>Cargo Vessels</i>			
	R2 Score	MAE	MSE	Mean Err.	25 th Pct.	50 th Pct.	75 th Pct.	Std. Dev.
A1/C1	98.32%	0.0794	0.0219	13.0609	4.1290	8.1360	15.6287	16.8534
A1/C2	98.39%	0.0738	0.0207	12.0751	3.2538	7.2295	14.3310	16.7377
A1/C3	97.65%	0.0790	0.0263	12.6353	2.6082	6.5676	15.2610	18.7873
A1/C4	97.96%	0.0755	0.0241	12.1253	2.3751	6.1875	14.6569	18.3074
A1/C5	97.43%	0.0844	0.0290	13.4349	2.9712	7.2248	16.2579	19.6830
<i>Probabilistic Features</i>					<i>Cargo Vessels</i>			
A2/C1	98.20%	0.0804	0.0297	13.8892	4.0198	8.8602	16.3392	21.7328
A2/C2	98.21%	0.0816	0.0292	13.9605	4.2302	9.1191	16.7682	21.3547
A2/C3	97.89%	0.0763	0.0346	12.7730	2.4753	6.2913	14.3849	24.7063
A2/C4	97.91%	0.0787	0.0354	13.2785	2.6182	6.6299	15.1287	24.9233
A2/C5	97.52%	0.0882	0.0418	14.9181	3.1329	7.7203	17.1389	26.7791
<i>Trigonometrical Features</i>					<i>Cargo Vessels</i>			
A3/C1	98.09%	0.0737	0.0315	12.5173	2.9758	6.6108	13.9366	23.4030
A3/C2	98.08%	0.0740	0.0323	12.5150	2.9509	6.6810	13.9237	23.8451
A3/C3	97.80%	0.0752	0.0376	12.7279	2.3615	6.0779	14.0855	26.1927
A3/C4	97.70%	0.0801	0.0397	13.5411	2.6477	6.6960	15.2335	26.7318
A3/C5	97.39%	0.0874	0.0448	14.8360	3.0500	7.5764	16.7728	28.1661

Table 4. Comparison of different forecasting models over Cargo vessels in the Gulf of St. Lawrence.

varying by half a kilometer to one kilometer. These results affirm that our model benefits from incorporating probabilistic features, particularly trigonometrical ones, leading to more accurate route approximation than the default features. Some models exhibit near-comparable results when analyzing the outcomes of using default features. Although the model may appear to be capable of replicating the intricate feature engineering we propose, it is important to note that these findings are not consistent across all metrics. Therefore, this behavior is an anomaly and may indicate potential constraints on the model generalization.

More specifically, in Table 4, the A1/C2 model showed the best performance under the default features for cargo vessels, with the lowest Mean Absolute Error (MAE) of 0.0738, Mean Squared Error (MSE) of 0.0207, Mean Error of 12.0751 km, and Standard Deviation of 16.7377 km. In the case of the probabilistic features, model A2/C3 marginally outperformed others, achieving the lowest Mean Error of 12.7730 km and 25th percentile error of 2.4753 km, while model A2/C2 recorded the lowest MSE of 0.0292 and Standard Deviation of 21.3547 km. Among the trigonometric features, model A3/C1 showed the best results with the lowest MAE of 0.0737 and MSE of 0.0315, while model A3/C2 showed the lowest Mean Error of 12.5150 km. In Table 5, the B1/C2 model under default features exhibited the best performance for tankers, while under probabilistic features, the B2/C1 and B2/C2 models outperformed others in most

<i>Default Features</i>							<i>Tanker Vessels</i>	
	R2 Score	MAE	MSE	Mean Err.	25 th Pct.	50 th Pct.	75 th Pct.	Std. Dev.
B1/C1	98.17%	0.0751	0.0215	12.3757	3.9366	7.7236	14.5098	17.3276
B1/C2	98.32%	0.0691	0.0198	11.3193	3.0421	6.7370	13.4186	17.0405
B1/C3	97.10%	0.0747	0.0259	11.9052	2.4920	6.2030	14.2152	18.7462
B1/C4	97.74%	0.0707	0.0232	11.3954	2.2510	5.8280	13.5352	18.3798
B1/C5	96.92%	0.0799	0.0283	12.6215	2.7878	6.7369	15.0114	19.6633
<i>Probabilistic Features</i>							<i>Tanker Vessels</i>	
B2/C1	98.42%	0.0748	0.0242	12.9008	3.8051	8.4623	15.4267	19.5181
B2/C2	98.36%	0.0765	0.0242	13.0027	4.0693	8.6144	15.6594	19.3429
B2/C3	98.06%	0.0705	0.0293	11.7623	2.3384	5.9108	13.3525	22.8520
B2/C4	98.03%	0.0740	0.0307	12.4650	2.5137	6.3644	14.3824	23.2749
B2/C5	97.72%	0.0833	0.0348	14.0422	3.0119	7.4313	16.4624	24.2642
<i>Trigonometrical Features</i>							<i>Tanker Vessels</i>	
B3/C1	98.29%	0.0691	0.0260	11.6770	2.8218	6.2823	13.1752	21.2020
B3/C2	98.21%	0.0696	0.0277	11.7550	2.8866	6.4927	13.2350	22.1301
B3/C3	97.97%	0.0698	0.0321	11.7930	2.2478	5.7668	13.1974	24.3013
B3/C4	97.92%	0.0749	0.0332	12.6534	2.5354	6.3981	14.4932	24.4186
B3/C5	97.55%	0.0827	0.0384	13.9672	2.9248	7.2341	16.0181	25.9926

Table 5. Comparison of different forecasting models over Tanker vessels in the Gulf of St. Lawrence.

metrics, and model **B2/C3** depicted the lowest MAE of 0.0705 and Mean Error of 11.7623 km. Under the trigonometric features, model **B3/C1** showed the lowest values across most evaluation metrics, including MAE of 0.0691, MSE of 0.0260, Mean Error of 11.6770 km, and 75th percentile error of 13.1752 km.

Upon conducting a thorough examination of these various models, we can conclude that the complexity of the models varies based on the feature sets, vessel types, and individual model attributes. Nonetheless, despite these differences, the models consistently exhibited high-performance levels, with dissimilarities primarily arising from the preference for specific feature sets. Furthermore, our analysis unveiled a deeper facet of the models' capabilities beyond the raw performance statistics. The models engage in intricate decision-making processes when working with diverse feature sets. For example, the increased standard deviation observed for trigonometric and probabilistic features does not necessarily indicate poor performance. Rather, it represents a unique form of dynamic decision-making that results in complex, erratic, yet precise trajectory shapes (*i.e.*, routes) that may not be reflected in numerical consistency.

As further experiments, we designed and tested five different scenarios, which are illustrated in Figures 10, 11, 12, and 13. These scenarios aim to compare and validate the decision-making capability of different models and highlight that the evaluation metrics used for numerical analysis can be misleading in

certain cases. Figure 10 shows the results for model C1, Figure 11 corresponds to C2, Figure 12 represents C3, while Figure 13 displays the model C4. As for model C5, we did not provide a visual representation due to its limited performance. However, the detailed results for this model are available in Tables 4 and 5.

In Figure 10, we can observe the performance of the proposed model (C1) on three sets of distinct features. The image highlights two incorrect path decisions made when using the Default Features, which are images 1(a) and 4(a). Additionally, it shows poor forecasting performance in image 5(a). However, the other two feature sets exhibit perfect path decisions, with clear variations in the approximation of the forecasted path with the observed ones. In this case, the Trigonometrical Features are better suited for approximating image 4(c) than the Probabilistic Features as seen in image 4(b). In contrast, the

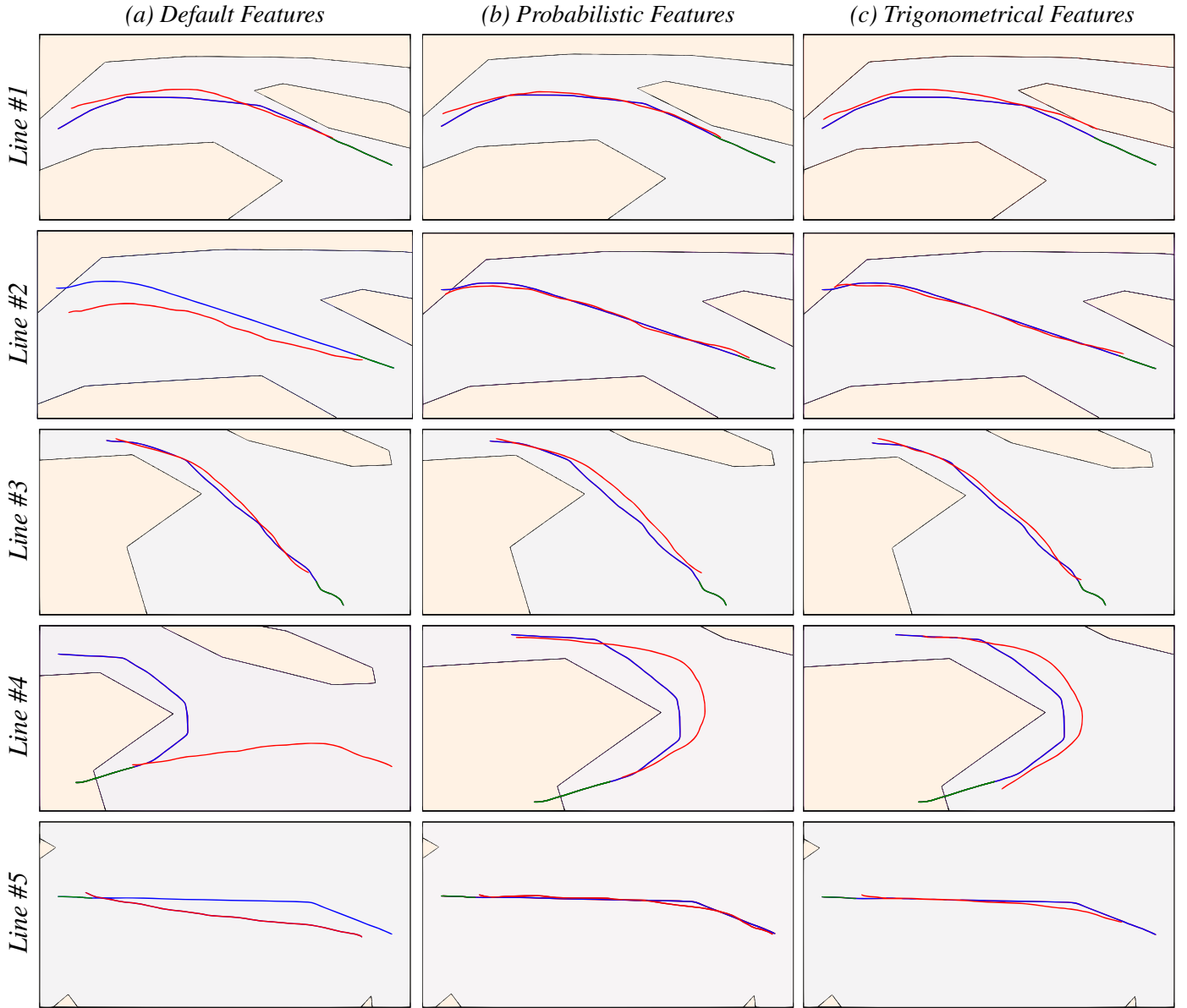


Figure 10. Proposed Model **with** *Convolutional Layers and Positional-Aware Attention* (C1). **Green** lines represent the input data, **Blue** the ground-truth, and **Red** the model forecasting.

Probabilistic Features are better for image **4(b)**, albeit with a broader curve shape that increases the error.

In Figure 11, the proposed model is shown without the CNN layers (C2). It is evident that the lack of these layers for spatial feature extraction produces a more noisy approximation of several paths. Specifically, the **1(b)/1(c)** and **2(b)/2(c)** paths from the Probabilistic and Trigonometrical Features are poorly fitted. The previously well-fitted, curvy-shaped forecast for the Probabilistic Features is now loosely related to the input trajectory and the expected forecasting, as seen in image **4(b)**. On the other hand, the Trigonometrical Features show a better curve fitting in image **5(c)**, yet with highly imperfect forecastings due to the loss of spatial features sourced from the stacked convolutional layers. Moreover, the default features still struggle to forecast the correct paths. Although there were minor improvements in

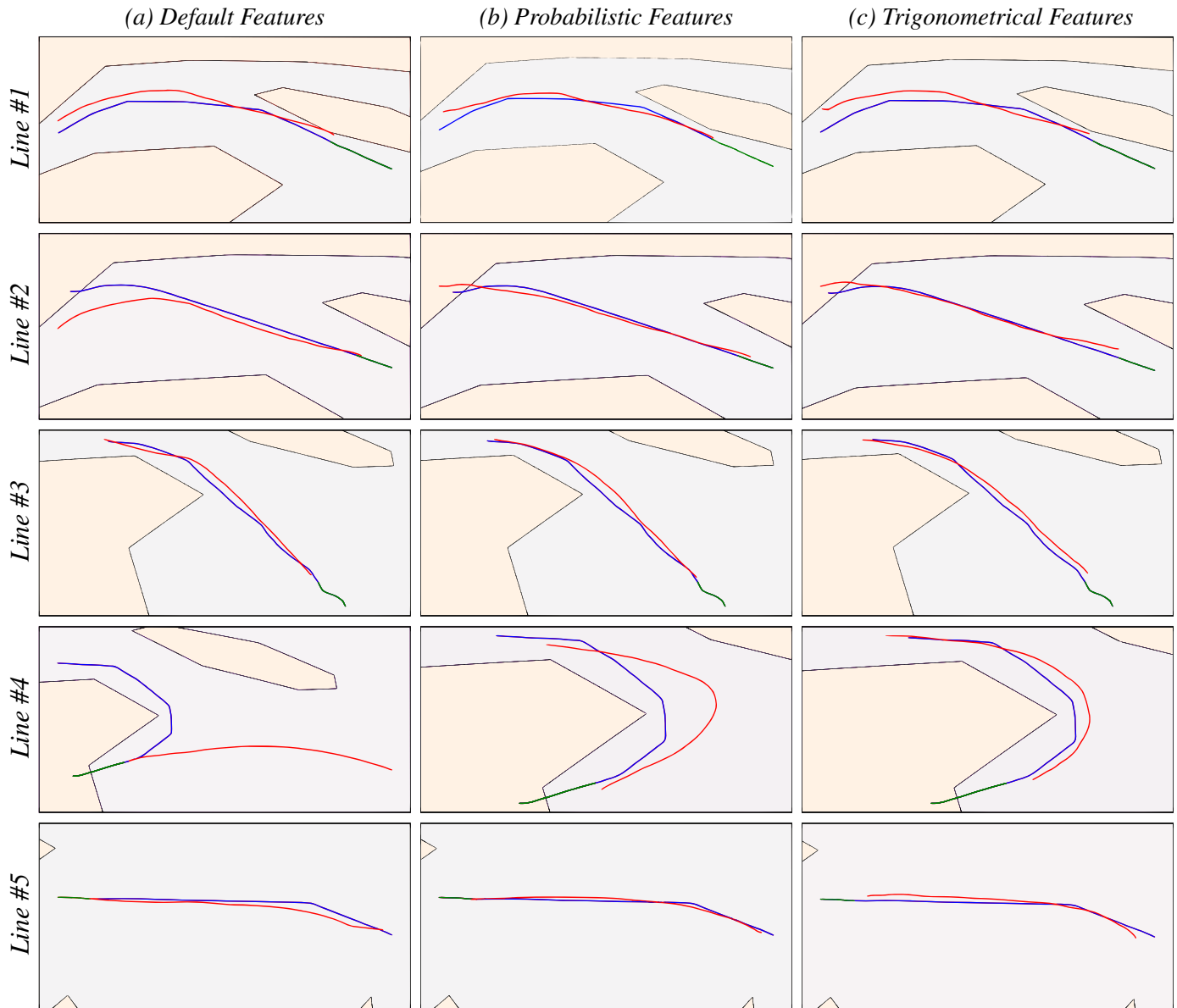


Figure 11. Proposed Model **with** *Convolutional Layers* and **without** *Positional-Aware Attention* (C2). **Green** lines represent the input data, **Blue** the ground-truth, and **Red** the model forecasting.

images $I(a)$ and $5(a)$, the curvy-shaped $4(a)$ and the port-entering one $2(a)$ remain incorrect.

The image in Figure 12 shows a slight change in the setup, where there is no attention mechanism, but instead, the stack of convolution layers (C3) is used. The image also reveals that all three sets of features fail equally to fit images $I(a)$, $I(b)$, and $I(c)$. This suggests that the model might be repeating a dominant pattern in the dataset, which results in failing to account for changes in the features required to predict the correct trajectory. On the other hand, images $2(b)$ and $2(c)$, which depict a port entry, are correctly predicted for both Probabilistic and Trigonometrical features. However, for the Default Features in image $2(a)$, it shows the worst result seen so far. Interestingly, the Trigonometrical Features are extremely well-fitted to the curvy-shape pattern, reasonably fitted by the Probabilistic Features, and somewhat fitted

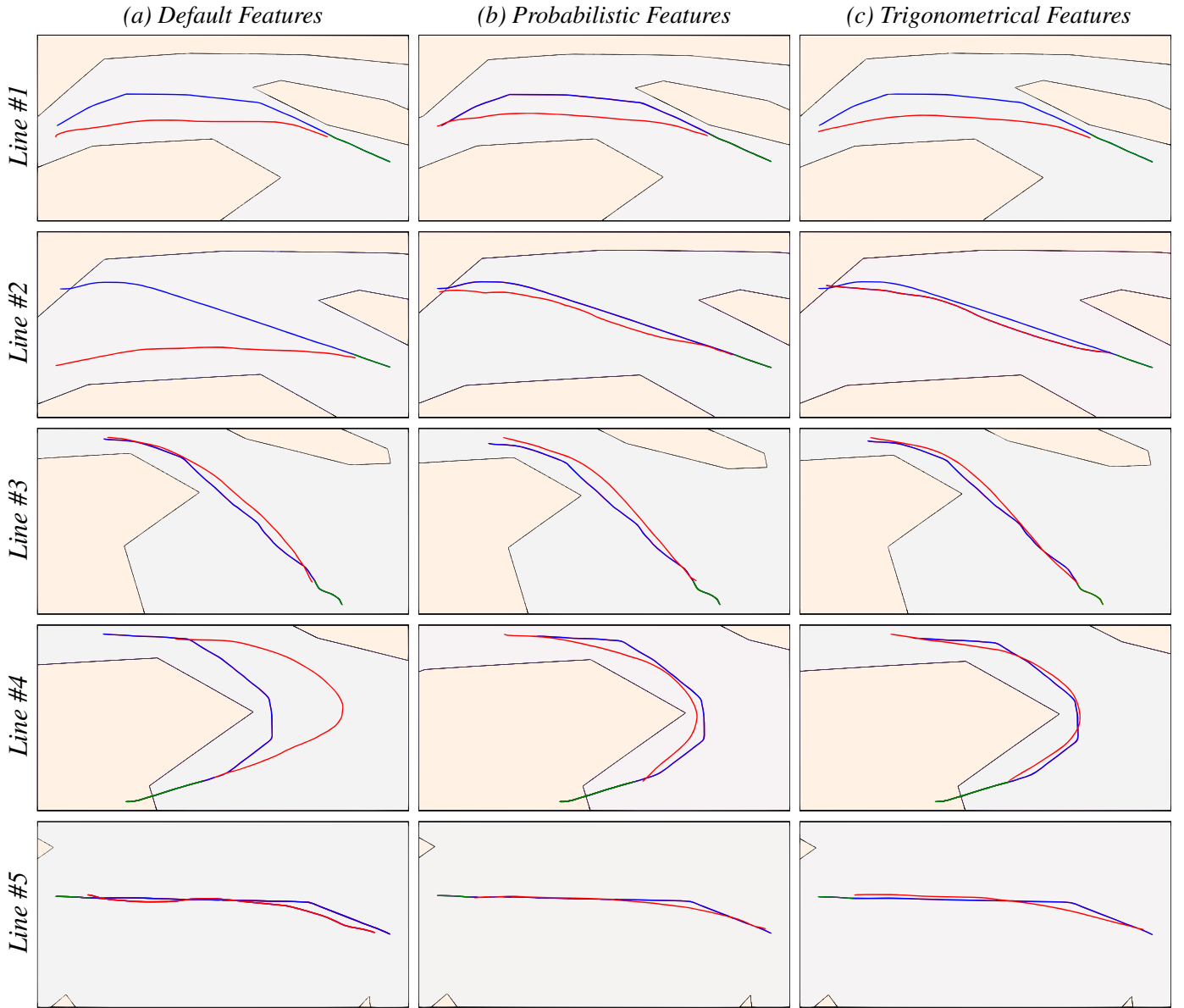


Figure 12. Proposed Model **without** Convolutional Layers and **with** Positional-Aware Attention (C3). **Green** lines represent the input data, **Blue** the ground-truth, and **Red** the model forecasting.

by the Default Features, images **4(c)**, **4(b)**, and **4(a)**, respectively. This indicates that spatial patterns play a larger role in this set of experiments, but it can lead to an overfitting scenario as CNNs tend to repeat dominant patterns from the training dataset. In the complete model with all layers intact (**C1**), the attention mechanism functions as a filter for the spatial features, helping to control overfitting in the forecasting.

In Figure 13, the probabilistic features, as seen in image **4(b)**, perform better in curvy-shaped forecasting when compared to the trigonometrical features, as seen in image **4(c)**. However, all three feature sets fail to provide accurate information for the forecasting of images **1(a)**, **1(b)**, and **1(c)**. Similarly, the default features fail to forecast images **2(a)** and **4(a)**. Although image **5(a)** moves in the correct direction, it fails to fit accurately as the other two sets of features managed to achieve in images **5(b)** and **5(c)**.

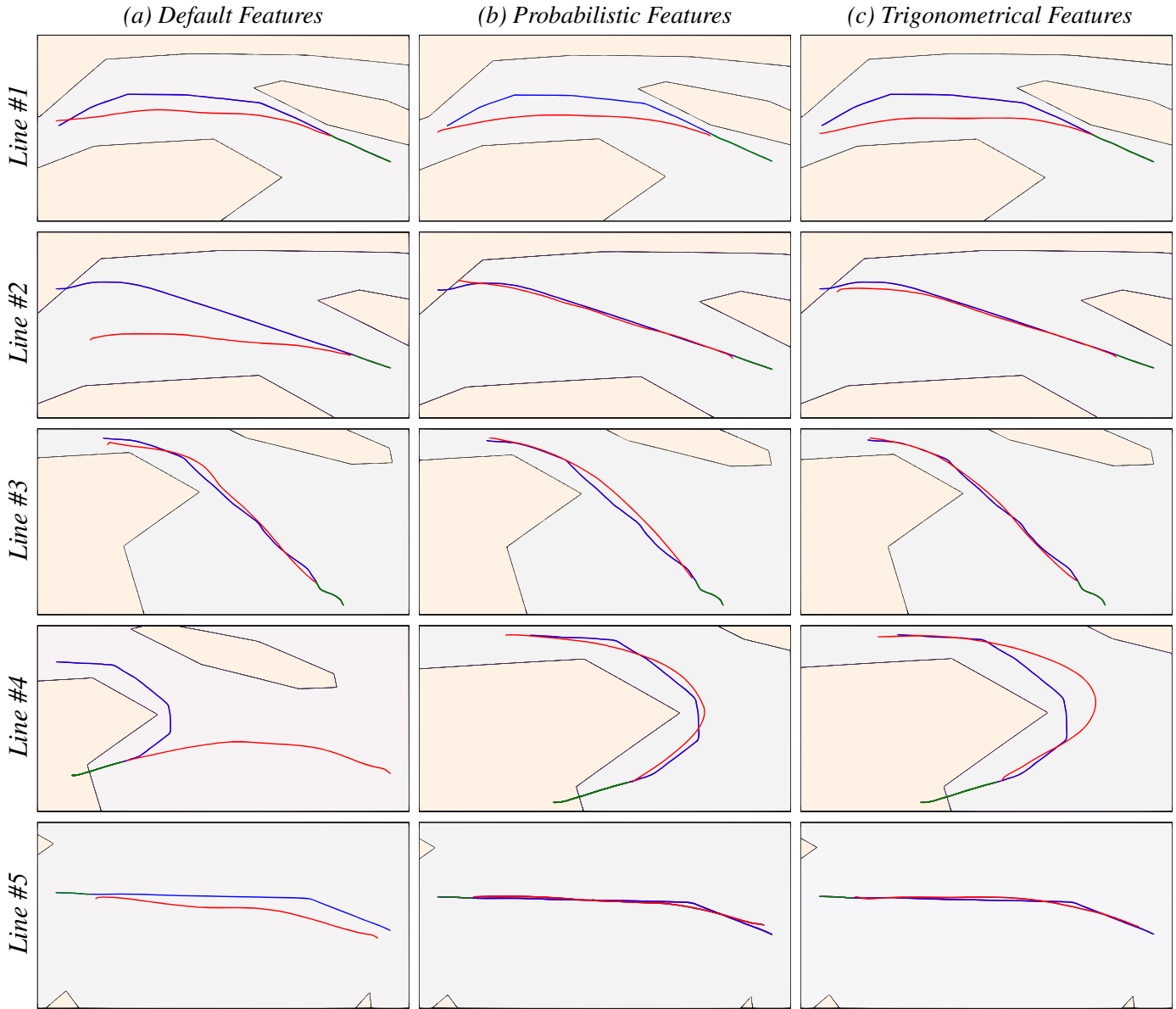


Figure 13. Proposed Model **without** *Convolutional Layers and Positional-Aware Attention* (**C4**).

Green lines represent the input data, **Blue** the ground-truth, and **Red** the model forecasting.

Our set of experiments shows that the numerical variations in Tables 4 and 5 reflect the partial performance of the models in terms of long-term multi-path trajectory forecasting. Such discrepancy arises as the assessment metrics often fail to capture the inherent decision-making complexity of the deep-learning models, especially in scenarios involving predominantly linear trajectories. Even when the dataset is balanced and stratified, these metrics require additional inspection to fully appreciate the models' ability to handle complex tasks. Moreover, the plethora of experiments has permitted us to identify the superior model for this study - model C1, trained on trigonometrical features. This model is proficient in accurately forecasting and visually representing all possible trajectories. In addition, the model performs better, yielding lower errors when trained on trigonometric features instead of probabilistic features. Therefore, the C1 model demonstrates superior path-decision capabilities, supported by the minimal approximation errors observed across the complete dataset of reserved vessels used for validation.

Discussions

Our research contributes to trajectory forecasting by introducing a spatio-temporal model that integrates probabilistic feature engineering with deep learning techniques. This approach enables the model to identify intricate route patterns and make informed decisions that simpler baseline models often overlook. Our model can accurately predict straight and curved trajectories, including path changes, significantly improving long-term vessel trajectory forecasting. We tested the model in various conditions with multiple feature sets and vessel types. The results showed its robustness and universality in different contexts.

We want to emphasize that relying solely on numerical indicators can be misleading when making decisions in complex scenarios. Our model is efficient in making correct long-term path decisions, even though it may not always be as straight as baseline models due to its noisiness. On a practical level, the positional-aware attention mechanism in our deep-learning model significantly improves its ability to capture short- and long-term dependencies in vessel trajectories. This aspect enables the model to better interpret and forecast nuanced temporal patterns, resulting in improved trajectory-fitting capabilities.

Equally important to our study is its practical implications concerning maritime safety and preserving biodiversity. Improved trajectory forecasting can significantly enhance navigational safety. More importantly, it opens possibilities to prevent unintentional harm to marine life, particularly endangered species inhabiting busy sea routes such as the North Atlantic Right Whales (NARW). Our efforts motivate future investigations to augment model performance, including adding more route polygons across the Gulf of St. Lawrence for enhanced vessel path decisions, as well as exploring techniques like Dynamic Time Warping (DTW) as a loss function that could benefit the model robustness and generate less noisy trajectories.

In conclusion, by integrating probabilistic and trigonometric features, our model offers a foundation to harness the potential of sophisticated forecasting models, advancing maritime safety and proactively addressing ecological preservation concerns. The Automatic Identification System Database (AISdb) is the key to achieving reproducible and consistent results across our experiments. It aided in developing models

that are robust and adaptable to environmental variations. Our approach, combined with the efficient and flexible data processing capability of AISdb, sets a positive precedent for fostering reproducible research in vessel trajectory forecasting for the broader scientific community while harnessing the potential of deep learning models, advancing maritime safety, and proactively addressing ecological preservation concerns.

Methods

Dataset Description

Our dataset was collected from satellite-based Automatic Identification System (AIS) messages sent by vessels operating in the Gulf of St. Lawrence between 2015 and 2020. The AIS data was shared by Spire⁸, and it provides detailed records, including identification number, speed, location, vessel type, and timestamps. Table 6 outlines the total number of unique Cargo and Tanker vessels observed during these years. A total of 2409 unique Cargo vessels and 1040 unique Tanker vessels were recorded.

Table 6. Occurrence of Unique Vessels over each year.

	Total	2015	2016	2017	2018	2019	2020
Cargo	2409	897	748	703	800	723	741
Tanker	1040	301	292	279	314	280	266

Our final dataset, after the curation process, included 953 Cargo and 391 Tanker vessels for training, 51 Cargo and 21 Tanker vessels for validation, and 252 Cargo and 103 Tanker vessels for testing. The testing subset represents 20% of the entire dataset, while the validation subset (for deep-learning use) represents 20% of the non-testing data, and the outstanding data of this process constitutes the training dataset.

Automatic Identification System Database (AISdb)

The Marine Environmental Research Infrastructure for Data Integration and Application Network (MERIDIAN)⁹ leads the AISdb¹⁰ project, which brings together ocean researchers, computer scientists, and data managers. The project's primary objective is to create a resilient research data infrastructure that caters to the diverse needs of the global ocean science community. AISdb is a specialized platform developed to work with Automatic Identification System (AIS) data. AISdb is open-source software that offers a comprehensive toolkit for collecting and processing such data. It supports live streaming and historical raw AIS data files, making it a versatile solution for different data management requirements. AISdb's core functionality relies on SQLite and Postgres databases, which can be used locally or remotely through a Python interface that enables querying, data processing, visualization, and curated data exportation.

⁸ See <https://spire.com>.

⁹ See <https://meridian.cs.dal.ca>.

¹⁰ See <https://aisdb.meridian.cs.dal.ca/doc>.

AISdb is a powerful platform that provides an easy-to-use integration of AIS data with a wide range of environmental data stored in raster file formats. This integration is facilitated by the platform's built-in functions, which allow users to conveniently download ocean bathymetric chart grids and query the depth of the sea floor beneath each surface vessel position. The platform is designed to accommodate any raster data based on a longitude/latitude coordinate grid-cell system, enabling users to merge various environmental data sources with AIS data. This provides a more comprehensive understanding of vessel movements and interactions with the marine environment, including factors such as temperature, salinity, and water quality. By offering such a wide range of features and capabilities, AISdb empowers users to conduct advanced research and analysis in the marine domain – ideal for academic and industry use.

AISdb has taken a significant step in aiding the research community by making available a considerable portion of Canadian AIS data from January 2012 till the present¹¹, along with new monthly data releases. These data are available in raw, unparsed, and CSV format, making them easily accessible to researchers involved in AIS-data research. This initiative is meant to benefit the research groups that are already involved in AIS-data research or those interested in engaging in it in the future. The availability of raw and unparsed data eliminates the need for preprocessing and preparing key data for various ocean-related AIS-driven tasks, thus making the research process more streamlined and efficient.

AISdb enables the reproducibility of AIS-related research, and due to its Python interface, it enables users to leverage machine and deep learning algorithms for vessel-task modeling. In such a sense, this research was made available in the AISdb platform, so any interested party can use AISdb to reproduce the results and scale up or down the research we have done using their own or our freely available data.

Algorithm for Grid-Cell Probability

Our model for trajectory feature engineering is probabilistic. Its main objective is to predict the vessel's most likely future location based on the current position, direction data, and historical AIS data. We require the ocean to be segmented into deterministic grids to achieve this. These grids integrate the movement patterns of various vessels over time based on their position data from historical AIS records. Each cell in the grid records when and how frequently vessels have visited that particular cell, storing their motion statistics along with it. The model operates on two levels. Firstly, it predicts the vessel's route along the trajectory. Secondly, it also predicts the most likely end-grid-cell, which represents the completion of the vessel's journey. These two grid-cells are represented in terms of their centroids, which are calculated for each AIS message in the vessel trajectory separately. The step-by-step procedure to find possible routes and destinations for a new track (τ_n) is provided in Algorithm 1, which requires as input: C_i , $S_{\tau_n}^{C_i}$, and k .

Herein, C_i is the grid-cell related the current position of a vessel; $S_{\tau_n}^{C_i}$ is an attribute S_{τ_n} (*i.e.*, vessel density) from a track in grid-cell C_i ; lastly, k represents the number of top probable destinations to consider. In Line 2, T_{C_i} is a set of tuples containing historical vessel movement statistics of grid-cell C_i . We gather all potential destinations C_{dest} for each track T_{C_i} in Line 3. In Line 4, statistics S_τ of each historical track τ

¹¹ See <https://meridian.cs.dal.ca/vessel-tracking-data>.

Algorithm 1 Calculate Grid-cell Probability

Require: C_i current grid-cell of new track τ_n ; $S_{\tau_n}^{C_i}$ statistics of a new track $\tau_n \in C_i$; k number of destinations;

```
1: function POSSIBLE-DESTINATION( $C_i, S_{\tau_n}^{C_i}, k$ )
2:    $T_{C_i} = \{\tau | \tau_{C_i} = C_i, \tau \in \tilde{\mathbf{M}}\}$ 
3:    $C_{dest} = \{D_j | D_j \in \tau, \tau \in T_{C_i}\}$ 
4:    $S_{C_i} = \{S_\tau | \tau \in T_{C_i}\}$ 
5:    $\mathbf{D} = \phi$ 
6:   for  $S_{\tau_i} \in S_{C_i}$  do
7:      $e = \text{Euclidean}(S_{\tau_i}, S_{\tau_n}^{C_i})$ 
8:      $\mathbf{D} = \mathbf{D} \cup (S_{\tau_i} \rightarrow e)$ 
9:   end for
10:   $CD = \phi$ 
11:  for  $D_i \in C_{dest}$  do
12:     $D_i^{min} = \min \{dist | (S \rightarrow dist) \in \mathbf{D}, D_j \leftarrow S, D_j = D_i\}$ 
13:     $CD = CD \cup (D_i \rightarrow D_i^{min})$ 
14:  end for
15:   $\delta = \mu(D_i^{min} \in CD)$ 
16:   $CD_{updated} = \phi$ 
17:  for  $D_i \in C_{dest}$  do
18:     $D_i^{min} = D_i \in CD$ 
19:    if  $D_i^{min} < \delta$  then
20:       $prob_{cx} = \frac{||\{\tau | \tau \in T_{C_i}, D_j \leftarrow \tau, D_j = D_i\}||}{|T_{C_i}|}$ 
21:       $dist_i = D_i^{min} \times (1 - prob_{cx})$ 
22:       $CD_{updated} = CD_{updated} \cup (D_i \rightarrow dist_i)$ 
23:    end if
24:  end for
25:  return  $\{f : D_i | (D_i \leftarrow dist_i) \in CD_{updated}, dist_j > dist_i, j \neq i, i = 1, \dots, k\}$ 
26: end function
```

is calculated. In Line 5, we initialize the set D as an empty set. Subsequently, we calculated the similarity between each historical track and the new track in the current cell. The distance for each historical track (moving to a particular destination D_j) is stored in D . Lines 5–8 depicts the procedure where for each historical track's statistics $S_{\tau_i}^{C_i}$, we calculate the Euclidean distance, labeled as e , between S_{τ_i} and $S_{\tau_n}^{C_i}$. In the historical tracks, more than one track may pass through C_i to a particular destination D_j . Thus, for each unique $D_j \in C_{dest}$, we consider the track to have minimum distance with a historical track within the grid-cell. Lines 10–14 depicts this procedure where we calculate the minimum Euclidean (*i.e.*, inline

or L2) distance D_i^{min} to each destination cell D_i , which are recorded in the pair set CD . The mean (μ) of the population's minimum distances in CD is determined in Line 15. In the CD , we only consider those destination D_j whose distance is less than the mean (see Equation (4)). Line 16-23 depicts the procedure to store the score in $CD_{updated}$. The score is calculated by multiplying the similarity score and probability tracking passing cell C_i to reach a particular D_i . After processing, the function returns a set of tuples. Each tuple is uniquely identified by a pair of indices (i, j) , where $i \in [1, k]$ and j denote the tuple's rank.

Evaluation metrics

When evaluating the performance of a probabilistic model, three metrics are used: *Precision*, *Recall*, and *F1 Score*. *Precision* measures the model's ability to accurately identify only the relevant instances and is calculated by dividing true positive (TP) predictions by the sum of true positives and false positives (FP). *Recall*, also known as sensitivity, measures the model's ability to identify all relevant instances and is calculated by dividing true positives by the sum of true positives and false negatives (FN). *F1 Score* is a performance assessment metric that combines both *Precision* and *Recall*, giving a more comprehensive evaluation of the model's performance by taking the harmonic mean between these two values. To ensure a fair measure of model performance, each of these metrics is evaluated in a weighted manner.

$$Precision = \frac{TP}{TP + FP} \quad (17) \quad Recall = \frac{TP}{TP + FN} \quad (18) \quad F1 \text{ Score} = 2 \times \frac{Precision \times Recall}{Precision + Recall} \quad (19)$$

To evaluate the performance of our deep-learning model, we used: Mean Absolute Error – MAE, Mean Squared Error – MSE, and Coefficient of Determination – R^2 . The MAE measures the average size of errors in a set of predictions. It is calculated as the average of the absolute differences between the predicted and actual observations. Each difference carries equal weight. The MAE is derived from the number of observations (n), the actual observations (y_i), and the predicted observations (\hat{y}_i). The MSE measures the average of the squares of the errors. It is a quality measure of an estimator, representing the average squared difference between the estimated values and the actual value. The MSE is always non-negative, and lower values are better. The R^2 score is a statistical measure that shows the proportion of the variance in a dependent variable that is explained by one or more independent variables in a regression model. It indicates the goodness-of-fit of the model and how well-unseen samples are likely to be predicted. The value of R^2 ranges from 0 to 1, where 1 indicates the linear regression fits the data perfectly, and 0 indicates that the average is a better predictor. In this case, \bar{y} represents the mean of the observed data.

$$MAE = \frac{1}{n} \sum_{i=1}^n |y_i - \hat{y}_i| \quad (20) \quad MSE = \frac{1}{n} \sum_{i=1}^n (y_i - \hat{y}_i)^2 \quad (21) \quad R^2 = 1 - \frac{\sum_{i=1}^n (y_i - \hat{y}_i)^2}{\sum_{i=1}^n (y_i - \bar{y})^2} \quad (22)$$

Haversine distance

The distance between two AIS messages on the surface of the earth can be determined by the distance between the coordinates of $a, b \in \tau_i$ using the law of cosines from spherical trigonometry⁶⁰ (i.e., great

circle distance). The Equation 23 takes into account the latitudes \mathcal{L}_{at}^a and \mathcal{L}_{at}^b , the difference $\Delta_{ab}^{\mathcal{L}_{on}}$ between the longitudes \mathcal{L}_{on}^a and \mathcal{L}_{on}^b , and the Earth's radius \mathbf{R} (6,371 km), values are given in radians.

$$\mathbb{D}(a, b) = \left(\sin(\mathcal{L}_{at}^a) \times \sin(\mathcal{L}_{at}^b) + \cos(\mathcal{L}_{at}^a) \times \cos(\mathcal{L}_{at}^b) \times \cos(\Delta_{ab}^{\mathcal{L}_{on}}) \right) \times \mathbf{R} \quad (23)$$

Speed and Acceleration

The speed of a vessel is given by the ratio of distance with respect to the time to reach point a from b :

$$S(b, a) = \frac{\mathbb{D}(a, b)}{(time_b - time_a)} \quad (24)$$

Furthermore, we refer to acceleration as the change in speed between locations, calculated as $\Delta_S = S_2 - S_1$.

Bearing

The *bearing* is the direction of a vessel during its trajectory relative to the earth's surface, calculated as:

$$\theta(a, b) = \text{atan}_2 \left(\sin(\Delta_{\mathcal{L}_{on}}) \times \cos(\mathcal{L}_{at}^b), \right. \\ \left. \cos(\mathcal{L}_{at}^a) \times \sin(\mathcal{L}_{at}^b) - \sin(\mathcal{L}_{at}^a) \times \cos(\mathcal{L}_{at}^b) \times \cos(\Delta_{\mathcal{L}_{on}}) \right) \quad (25)$$

where $\Delta_{\mathcal{L}_{on}}$ is the difference between the longitudes of two points, $(\mathcal{L}_{on}^b - \mathcal{L}_{on}^a)$. Furthermore, the rate of bearing Δ_θ is defined as the difference between two bearing values $(\Delta_\theta = \theta_2 - \theta_1)$, adjusted to lie in the range of $[-180, 180]$ by adding or subtracting 360 from Δ_θ as needed.

Sliding window

The sliding window technique is commonly used in time series forecasting. It involves creating a moving frame or *window* of data that captures consecutive time steps. This window slides over the data, generating several adjacent input-output sequence pairs that can be used to train the model. If we have a time series of data represented by $\mathbf{x} = [x_1, x_2, \dots, x_N]$, a window of size n moves over the data and produces pairs as:

$$(x_i, x_{i+1}, \dots, x_{i+n-1}) \rightarrow x_{i+n}, \quad \forall i \in [1, N - n]. \quad (26)$$

The model predicts the value of the next time step, which is denoted as \hat{x}_{i+n} (or multiple time steps, as in our case), based on the input sequence of the previous time steps $(x_i, x_{i+1}, \dots, x_{i+n-1})$. The known output value x_{i+n} is used to evaluate and learn the predicted value. This sliding window technique helps to maintain and encapsulate the temporal sequence within the training samples, which makes it easier to identify and learn the temporal patterns for trajectory forecasting. The size of the window n , movement step size, and overlap factor can be adjusted to balance complexity and forecasting performance. In our case, we have pre-set an input of 1 to 3 hours, i.e., 6 to 18 AIS messages; and an output of 12 hours, i.e., 72 AIS messages. Due to the problem formulation we previously placed, these parameters were not adjusted.

Optimization strategy

The optimization function we use encapsulates the strategy of independently minimizing the Mean Absolute Error (MAE) for both output components, latitude, and longitude, such as formalized below:

$$\min_{\Theta} \left(\frac{1}{N} \sum_{i=1}^N \left| \mathcal{L}_{at}^i - \widehat{\mathcal{L}}_{at}^i \right| + \frac{1}{N} \sum_{j=1}^N \left| \mathcal{L}_{on}^j - \widehat{\mathcal{L}}_{on}^j \right| \right) \quad (27)$$

Here, $y = \langle \mathcal{L}_{at}, \mathcal{L}_{on} \rangle$ symbolizes the original coordinates, and $\hat{y} = \langle \widehat{\mathcal{L}}_{at}, \widehat{\mathcal{L}}_{on} \rangle$ symbolizes the predicted ones, while Θ stands as representation of the network parameters. For the optimization, we utilize the Adam optimizer with an initial learning rate set to $1e^{-3}$ combined with a weight decay parameter set to $1e^{-4}$ to prevent overfitting. To enhance this, we also employed a dynamic learning rate adjustment and early stopping strategy. The *Dynamic Learning Rate Adjustment* adapts the learning rate based on recent model performance. If the validation loss fails to improve for a specified number of epochs, the learning rate is reduced by a pre-set factor. Here, if no improvement is observed after 10 epochs, the learning rate is reduced by 25%. The monitoring re-starts after each reduction, while the learning rate is greater than zero. The *Early Stopping* terminates the learning process if the model fails to improve after a specified number of epochs, thus preventing overfitting. In this study, we stop the learning process if the validation loss fails to improve significantly after 30 epochs. These techniques ensure a harmonious balance between computational efficiency and model performance and prevent the overuse of computational resources.

Model hyperparameters

In the construction of the deep-learning model, various hyperparameters were utilized consistently across all experiments with the aim of enabling an unbiased evaluation. A regularization strength of 0.0005 was enforced for L2 Regularization. Various numbers of filter sizes (256, 256, 128) and kernel sizes (7, 5, 5) were employed within the framework of incremental convolutional blocks, with each of these blocks being subject to the stipulated L2 regularization. A Dropout Layer was instituted with a probability rate set at 10%. Within the Encoder and Decoder architecture, Bidirectional Long-Short Term Memory (Bi-LSTM) layers were used, each with 128 cells. Both the kernel and the recurrent weights in these layers were applied with the ReLU activation function and L2 regularization. Further, a Position-Aware Attention Mechanism was incorporated in order to enhance the model's attention to the input data's temporal sequence. To this end, a time factor of 1.25 was employed, resulting in a balance between self-attention and the capturing of longer-term dependencies within the data sequence. After the decoder, three dense layers were sequentially stacked. These layers were initiated with a decreasing number of neurons (128, 128, 64), and each was activated by the ReLU function. Consistently implementing these hyperparameters throughout all the experiments ensured we maintained an unbiased evaluation environment.

Computing environment

The experiments conducted on probabilistic and deep-learning models for trajectory forecasting were carried out in a high-performance computing environment. The environment was equipped with an

NVIDIA A100 GPU with 40GB of memory, further complemented by 42 CPUs with 128GB of RAM. This allowed for efficient data processing and model training, reducing time lags and enabling comprehensive exploration of the machine-learning models within a reasonable time frame.

References

1. Organization, I. M. Brief history of imo. <https://www.imo.org/en/About/HistoryOfIMO/Pages/Default.aspx>. Accessed: 17th October 2022.
2. Organization, I. M. Ais transponders. <https://www.imo.org/en/OurWork/Safety/Pages/AIS.aspx>. Accessed: 17th October 2022.
3. Fournier, M., Casey Hilliard, R., Rezaee, S. & Pelot, R. Past, present, and future of the satellite-based automatic identification system: Areas of applications (2004–2016). *WMU journal maritime affairs* **17**, 311–345 (2018).
4. Goerlandt, F. & Kujala, P. Traffic simulation based ship collision probability modeling. *Reliab. Eng. & Syst. Saf.* **96**, 91–107, DOI: [10.1016/j.ress.2010.09.003](https://doi.org/10.1016/j.ress.2010.09.003) (2011). Special Issue on Safecomp 2008.
5. Chen, P., Huang, Y., Mou, J. & van Gelder, P. Probabilistic risk analysis for ship-ship collision: State-of-the-art. *Saf. Sci.* **117**, 108–122, DOI: [10.1016/j.ssci.2019.04.014](https://doi.org/10.1016/j.ssci.2019.04.014) (2019).
6. Yang, D., Wu, L., Wang, S., Jia, H. & Li, K. X. How big data enriches maritime research—a critical review of automatic identification system (ais) data applications. *Transp. Rev.* **39**, 755–773 (2019).
7. Harati-Mokhtari, A., Wall, A., Brooks, P. & Wang, J. Automatic identification system (ais): data reliability and human error implications. *The J. Navig.* **60**, 373–389 (2007).
8. Millefiori, L. M. *et al.* Covid-19 impact on global maritime mobility. *Sci. reports* **11**, 1–16 (2021).
9. Karataş, G. B., Karagoz, P. & Ayran, O. Trajectory pattern extraction and anomaly detection for maritime vessels. *Internet Things* **16**, 100436 (2021).
10. Eljabu, L., Etemad, M. & Matwin, S. Anomaly detection in maritime domain based on spatio-temporal analysis of ais data using graph neural networks. In *2021 5th International Conference on Vision, Image and Signal Processing (ICVISIP)*, 142–147 (IEEE, 2021).
11. Capobianco, S., Millefiori, L. M., Forti, N., Braca, P. & Willett, P. Deep learning methods for vessel trajectory prediction based on recurrent neural networks. *IEEE Transactions on Aerosp. Electron. Syst.* **57**, 4329–4346 (2021).
12. Mustafa, H., Barrus, C., Leal, E. & Gruenwald, L. Gtraculus: A local trajectory clustering algorithm for gpus. In *2021 IEEE 37th International Conference on Data Engineering Workshops (ICDEW)*, 30–35 (IEEE, 2021).
13. Rong, H., Teixeira, A. & Soares, C. G. Data mining approach to shipping route characterization and anomaly detection based on ais data. *Ocean. Eng.* **198**, 106936 (2020).

14. Fu, P., Wang, H., Liu, K., Hu, X. & Zhang, H. Finding abnormal vessel trajectories using feature learning. *IEEE Access* **5**, 7898–7909 (2017).
15. Li, H. *et al.* Spatio-temporal vessel trajectory clustering based on data mapping and density. *IEEE Access* **6**, 58939–58954 (2018).
16. Haranwala, Y. J., Spadon, G., Renso, C. & Soares, A. A data augmentation algorithm for trajectory data. In *1st ACM SIGSPATIAL International Workshop on Methods for Enriched Mobility Data: Emerging issues and Ethical perspectives 2023 (EMODE '23)*, 5, DOI: [10.1145/3615885.3628008](https://doi.org/10.1145/3615885.3628008) (ACM, New York, NY, USA, New York, NY, USA, 2023).
17. Wang, C., Ren, H. & Li, H. Vessel trajectory prediction based on ais data and bidirectional gru. In *2020 International Conference on Computer Vision, Image and Deep Learning (CVIDL)*, 260–264 (IEEE, 2020).
18. Park, J., Jeong, J. & Park, Y. Ship trajectory prediction based on bi-lstm using spectral-clustered ais data. *J. Mar. Sci. Eng.* **9**, 1037 (2021).
19. Murray, B. & Perera, L. P. A dual linear autoencoder approach for vessel trajectory prediction using historical ais data. *Ocean. Eng.* **209**, 107478, DOI: [10.1016/j.oceaneng.2020.107478](https://doi.org/10.1016/j.oceaneng.2020.107478) (2020).
20. Campbell, J. N., Isenor, A. W. & Ferreira, M. D. Detection of invalid ais messages using machine learning techniques. *Procedia Comput. Sci.* **205**, 229–238 (2022).
21. Spadon, G., Ferreira, M. D., Soares, A. & Matwin, S. Unfolding ais transmission behavior for vessel movement modeling on noisy data leveraging machine learning. *IEEE Access* (2022).
22. Peng, Z. *et al.* Establishment of inland ship air pollution emission inventory based on power method correction model. *Sustainability* **14**, 11188 (2022).
23. Pichegru, L. *et al.* Maritime traffic trends around the southern tip of africa—did marine noise pollution contribute to the local penguins’ collapse? *Sci. The Total. Environ.* **849**, 157878 (2022).
24. Nguyen, D., Vadaine, R., Hajduch, G., Garelo, R. & Fablet, R. A multi-task deep learning architecture for maritime surveillance using ais data streams. In *2018 IEEE 5th International Conference on Data Science and Advanced Analytics (DSAA)*, 331–340 (IEEE, 2018).
25. Patmanidis, S., Voulgaris, I., Sarri, E., Papavassilopoulos, G. & Papavasileiou, G. Maritime surveillance, vessel route estimation and alerts using ais data. In *2016 24th Mediterranean Conference on Control and Automation (MED)*, 809–813 (IEEE, 2016).
26. Zhang, Y.-l., Peng, P.-f., Liu, J.-s. & Liu, S.-k. Ais data oriented ships’ trajectory mining and forecasting based on trajectory delimiter. In *2018 10th International Conference on Intelligent Human-Machine Systems and Cybernetics (IHMSC)*, vol. 1, 269–273 (IEEE, 2018).

27. Üney, M., Millefiori, L. M. & Braca, P. Data driven vessel trajectory forecasting using stochastic generative models. In *IEEE International Conference on Acoustics, Speech and Signal Processing (ICASSP)*, 8459–8463 (IEEE, 2019).
28. Faghih-Roohi, S., Xie, M. & Ng, K. M. Accident risk assessment in marine transportation via markov modeling and markov chain monte carlo simulation. *Ocean. engineering* **91**, 363–370 (2014).
29. Le Guillaume, N. & Lerouvreur, X. Unsupervised extraction of knowledge from s-ais data for maritime situational awareness. In *Proceedings of the 16th International Conference on Information Fusion*, 2025–2032 (IEEE, 2013).
30. d’Afflisio, E., Braca, P., Millefiori, L. M. & Willett, P. Maritime anomaly detection based on mean-reverting stochastic processes applied to a real-world scenario. In *2018 21st International Conference on Information Fusion (FUSION)*, 1171–1177 (IEEE, 2018).
31. Forti, N., Millefiori, L. M. & Braca, P. Unsupervised extraction of maritime patterns of life from automatic identification system data. In *OCEANS 2019-Marseille*, 1–5 (IEEE, 2019).
32. Forti, N., Millefiori, L. M., Braca, P. & Willett, P. Anomaly detection and tracking based on mean-reverting processes with unknown parameters. In *ICASSP 2019-2019 IEEE International Conference on Acoustics, Speech and Signal Processing (ICASSP)*, 8449–8453 (IEEE, 2019).
33. Ferreira, M. D., Spadon, G., Soares, A. & Matwin, S. A semi-supervised methodology for fishing activity detection using the geometry behind the trajectory of multiple vessels. *Sensors* **22**, 6063 (2022).
34. Newaliya, N. & Singh, Y. A review of maritime spatio-temporal data analytics. In *2021 International Conference on Computational Performance Evaluation (ComPE)*, 219–226 (IEEE, 2021).
35. Pallotta, G., Horn, S., Braca, P. & Bryan, K. Context-enhanced vessel prediction based on ornstein-uhlenbeck processes using historical ais traffic patterns: Real-world experimental results. In *17th international conference on information fusion (FUSION)*, 1–7 (IEEE, 2014).
36. Nguyen, D. & Fablet, R. TrAISformer-a generative transformer for AIS trajectory prediction. *CoRR abs/2109.03958* (2021). [2109.03958](https://arxiv.org/abs/2109.03958).
37. Lamb, A. M. *et al.* Professor forcing: A new algorithm for training recurrent networks. In Lee, D., Sugiyama, M., Luxburg, U., Guyon, I. & Garnett, R. (eds.) *Advances in Neural Information Processing Systems*, vol. 29 (Curran Associates, Inc., 2016).
38. Capobianco, S., Millefiori, L. M., Forti, N., Braca, P. & Willett, P. Deep learning methods for vessel trajectory prediction based on recurrent neural networks. *IEEE Transactions on Aerosp. Electron. Syst.* **57**, 4329–4346, DOI: [10.1109/TAES.2021.3096873](https://doi.org/10.1109/TAES.2021.3096873) (2021).

39. Capobianco, S., Forti, N., Millefiori, L. M., Braca, P. & Willett, P. Recurrent encoder-decoder networks for vessel trajectory prediction with uncertainty estimation. *IEEE Transactions on Aerosp. Electron. Syst.* 1–12, DOI: [10.1109/TAES.2022.3216823](https://doi.org/10.1109/TAES.2022.3216823) (2022).
40. O’Brien, O. *et al.* Repatriation of a historical north atlantic right whale habitat during an era of rapid climate change. *Sci. Reports* **12**, 1–10 (2022).
41. Spadon, G., Carvalho, A. C. d., Rodrigues-Jr, J. F. & Alves, L. G. Reconstructing commuters network using machine learning and urban indicators. *Sci. reports* **9**, 11801 (2019).
42. Lei, W., Alves, L. G. & Amaral, L. A. N. Forecasting the evolution of fast-changing transportation networks using machine learning. *Nat. communications* **13**, 4252 (2022).
43. Alves, L. G., Rybski, D. & Ribeiro, H. V. Commuting network effect on urban wealth scaling. *Sci. Reports* **11**, 22918 (2021).
44. Rodrigues-Jr, J. F., Gutierrez, M. A., Spadon, G., Brandoli, B. & Amer-Yahia, S. Lig-doctor: Efficient patient trajectory prediction using bidirectional minimal gated-recurrent networks. *Inf. Sci.* **545**, 813–827, DOI: [10.1016/j.ins.2020.09.024](https://doi.org/10.1016/j.ins.2020.09.024) (2021).
45. Rodrigues-Jr, J. F., Spadon, G., Brandoli, B. & Amer-Yahia, S. Patient trajectory prediction in the mimic-iii dataset, challenges and pitfalls. *CoRR* **abs/1909.04605** (2019). [1909.04605](https://arxiv.org/abs/1909.04605).
46. Spadon, G. *et al.* Pay attention to evolution: Time series forecasting with deep graph-evolution learning. *IEEE Transactions on Pattern Analysis Mach. Intell.* **44**, 5368–5384, DOI: [10.1109/TPAMI.2021.3076155](https://doi.org/10.1109/TPAMI.2021.3076155) (2022).
47. Spadon, G. *et al.* Behavioral characterization of criminality spread in cities. In *International Conference on Computational Science (ICCS)*, vol. 108, 2537–2541, DOI: [10.1016/J.PROCS.2017.05.118](https://doi.org/10.1016/J.PROCS.2017.05.118) (Elsevier, 2017).
48. Spadon, G., Gimenes, G. & Rodrigues-Jr, J. F. Identifying urban inconsistencies via street networks. *Procedia Comput. Sci.* **108**, 18–27, DOI: [10.1016/j.procs.2017.05.103](https://doi.org/10.1016/j.procs.2017.05.103) (2017). International Conference on Computational Science, ICCS 2017, 12–14 June 2017, Zurich, Switzerland.
49. Spadon, G., Gimenes, G. & Rodrigues, J. F. Topological street-network characterization through feature-vector and cluster analysis. In *Computational Science – ICCS 2018: 18th International Conference, Wuxi, China, June 11–13, 2018, Proceedings, Part I*, 274–287, DOI: [10.1007/978-3-319-93698-7_21](https://doi.org/10.1007/978-3-319-93698-7_21) (Springer-Verlag, Berlin, Heidelberg, 2018).
50. Spadon, G., Brandoli, B., Eler, D. M. & Rodrigues-Jr, J. F. Detecting multi-scale distance-based inconsistencies in cities through complex-networks. *J. Comput. Sci.* **30**, 209–222, DOI: [10.1016/j.jocs.2018.12.015](https://doi.org/10.1016/j.jocs.2018.12.015) (2019).

51. Huang Tang, Y. Y. & Shen, H. A model for vessel trajectory prediction based on long short-term memory neural network. *J. Mar. Eng. & Technol.* **21**, 136–145, DOI: [10.1080/20464177.2019.1665258](https://doi.org/10.1080/20464177.2019.1665258) (2022).
52. Suo, Y., Chen, W., Claramunt, C. & Yang, S. A ship trajectory prediction framework based on a recurrent neural network. *Sensors* **20**, DOI: [10.3390/s20185133](https://doi.org/10.3390/s20185133) (2020).
53. Ibadurrahman *et al.* Long-term ship position prediction using automatic identification system (ais) data and end-to-end deep learning. *Sensors* **21**, DOI: [10.3390/s21217169](https://doi.org/10.3390/s21217169) (2021).
54. Gao, M., Shi, G. & Li, S. Online prediction of ship behavior with automatic identification system sensor data using bidirectional long short-term memory recurrent neural network. *Sensors* **18**, DOI: [10.3390/s18124211](https://doi.org/10.3390/s18124211) (2018).
55. Bao, K. *et al.* An improved ship trajectory prediction based on ais data using mha-bigru. *J. Mar. Sci. Eng.* **10**, DOI: [10.3390/jmse10060804](https://doi.org/10.3390/jmse10060804) (2022).
56. Yang, C.-H., Wu, C.-H., Shao, J.-C., Wang, Y.-C. & Hsieh, C.-M. Ais-based intelligent vessel trajectory prediction using bi-lstm. *IEEE Access* **10**, 24302–24315, DOI: [10.1109/ACCESS.2022.3154812](https://doi.org/10.1109/ACCESS.2022.3154812) (2022).
57. Murray, B. & Perera, L. P. An ais-based deep learning framework for regional ship behavior prediction. *Reliab. Eng. & Syst. Saf.* **215**, 107819, DOI: [10.1016/j.ress.2021.107819](https://doi.org/10.1016/j.ress.2021.107819) (2021).
58. Liu, T. & Ma, J. Ship navigation behavior prediction based on ais data. *IEEE Access* **10**, 47997–48008, DOI: [10.1109/ACCESS.2022.3172308](https://doi.org/10.1109/ACCESS.2022.3172308) (2022).
59. Capobianco, S., Forti, N., Millefiori, L. M., Braca, P. & Willett, P. Uncertainty-aware recurrent encoder-decoder networks for vessel trajectory prediction. In *2021 IEEE 24th International Conference on Information Fusion (FUSION)*, 1–5, DOI: [10.23919/FUSION49465.2021.9626839](https://doi.org/10.23919/FUSION49465.2021.9626839) (2021).
60. Konstantopoulos, T. *Introduction to projective geometry*. September (Dover Publications, 2012).

Acknowledgments

This research was partially funded by the Natural Sciences and Engineering Research Council of Canada (NSERC), Grant number RGPIN-2022-03909; the Institute for Big Data Analytics (IBDA) and the Ocean Frontier Institute (OFI) at Dalhousie University, Halifax - NS, Canada; and further funded by the Canada First Research Excellence Fund (CFREF), the Canadian Foundation for Innovation MERIDIAN cyberinfrastructure. We thank all funding sources and *Spire* for providing the vessel trajectory dataset.

Author contributions statement

Conceptualization, G.S. and J.K.; methodology, G.S., J.K., R.P., and S.M.; AISdb software, G.S., J.K., M.S., S.V., R.G., R.P., and S.M.; validation, G.S., J.K., and A.S.; formal analysis, G.S.; data modeling,

G.S. and J.K.; model optimization, G.S.; AISdb integration, G.S., J.K.; data curation, G.S., J.K., D.E., and J.B.; writing — original draft preparation, G.S. and J.K.; writing — review and editing, all authors; visualization, G.S. and J.K.; supervision, R.F., R.P., S.M.; project administration, G.S.; funding acquisition, G.S., R.F., R.P., S.M.; All authors have read and agreed to the published version of the manuscript.

Competing interests

The authors declare no competing interests.